Effects of the microphysical equation of state in the mergers of magnetized neutron stars with neutrino cooling

Carlos Palenzuela,[1] Steven L. Liebling,[2] David Neilsen,[3] Luis Lehner,[4] O. L. Caballero,[5] Evan O'Connor,[6] and Matthew Anderson[7]

[1]*Departament de Física, Universitat de les Illes Balears and Institut d'Estudis Espacials de Catalunya, Palma de Mallorca, Baleares E-07122, Spain*
[2]*Department of Physics, Long Island University, Brookville, New York 11548, USA*
[3]*Department of Physics and Astronomy, Brigham Young University, Provo, Utah 84602, USA*
[4]*Perimeter Institute for Theoretical Physics, Waterloo, Ontario N2L 2Y5, Canada*
[5]*Department of Physics, University of Guelph, Guelph, Ontario N1G 2W1, Canada*
[6]*Department of Physics, North Carolina State University, Raleigh, North Carolina 27695, USA*
[7]*Pervasive Technology Institute, Indiana University, Bloomington, Indiana 47405, USA*

(Received 8 May 2015; published 25 August 2015)

We study the merger of binary neutron stars using different realistic, microphysical nuclear equations of state, as well as incorporating magnetic field and neutrino cooling effects. In particular, we concentrate on the influence of the equation of state on the gravitational wave signature and also on its role, in combination with cooling and electromagnetic effects, in determining the properties of the hypermassive neutron star resulting from the merger, the production of neutrinos, and the characteristics of ejecta from the system. The ejecta we find are consistent with other recent studies that find soft equations of state produce more ejecta than stiffer equations of state. Moreover, the degree of neutron richness increases for softer equations of state. In light of reported kilonova observations (associated to GRB 130603B and GRB 060614) and the discovery of relatively low abundances of heavy, radioactive elements in deep sea deposits (with respect to possible production via supernovae), we speculate that a soft equation of state (EOS) might be preferred—because of its significant production of sufficiently neutron rich ejecta—if such events are driven by binary neutron star mergers. We also find that realistic magnetic field strengths, obtained with a subgrid model tuned to capture magnetic amplification via the Kelvin-Helmholtz instability at merger, are generally too weak to affect the gravitational wave signature postmerger within a time scale of ≈ 10 ms but can have subtle effects on the postmerger dynamics.

DOI: 10.1103/PhysRevD.92.044045 PACS numbers: 04.25.D-, 97.60.Jd, 04.30.-w

I. INTRODUCTION

Binary neutron star systems (BNS) represent perhaps the most exciting and anticipated source for upcoming gravitational wave (GW) observations. In contrast to other expected binary sources such as neutron star–black hole binaries, BNS have been observed and these observations lead to reasonably robust lower bounds on the expected GW detections [1]. In addition, neutron stars, being made of matter and supporting strong magnetic fields, are more complicated than black holes, especially during merger. The coalescence of neutron stars, being a highly dynamical violent event, disrupts the stars, powers electromagnetic events, and produces large neutrino bursts. Other effects may produce precursor signals prior to merger through either the interaction of stellar magnetospheres [2–4] or crust cracking [5].

The merger produces a differentially rotating, hot massive neutron star (MNS) with a strong neutrino luminosity. Such mergers are suspected engines of short, gamma ray bursts (sGRB), arguably the most spectacular electromagnetic counterpart to a strong GW event. Binaries composed of a black hole and neutron star may also power sGRB, but, in order for such binaries to do so, either low mass ratios or black holes with significant spin are required, e.g. [6–9]. In both systems, the merger may produce a significant neutron rich ejecta which can trigger kilonova events [10] (see also [11–13]). Remarkably, a recent observation of a sGRB led to a follow-up observation in the infrared indicative of a kilonova event [14,15] and evidence for a second [16] has also been presented. This observation provides further support for the connection between nonvacuum binary mergers with sGRBs [17].

Moving beyond the broad expectations of BNS mergers sketched above, the detailed dynamics of such mergers depend on a number of parameters, such as the stellar masses, equation of state, and magnetization, to name but a few. Fortunately, the combined efforts by the astrophysics and numerical relativity communities are gradually refining our understanding of these systems and the observational opportunities they present. For instance, simulations have indicated that the merger will give rise to a black hole promptly when the total mass of the system $M_{\rm total} \gtrsim 2.8 M_{\odot}$ (e.g. [18,19]); provided an approximate range for the final spin of the black hole for cases that do collapse [20];

indicated that the collision can produce magnetic field strengths in the resulting MNS that range from magnetar levels to higher [21–23]; and contributed gravitational wave templates to aid in data analysis efforts (e.g. [24–26]).

Most recently, a number of research avenues are attracting considerable interest. A significant effort is examining possible electromagnetic counterparts, of which the aforementioned sGRB are just one example (see e.g. [2,27–31]. Another is the study of binaries with more realistic equations of state [24,32–34]. In particular, the hope is that information about the true equation of state for NS interiors can be obtained from observations. Related to such efforts is an intense interest in ejecta and outflows [34,35], because of their connection to possible kilonova events and their role in explaining the origin of r-process elements [36]. Neutron star binary characteristics, including ejecta, have also been actively studied within Newtonian models [37], where the dynamics sometimes exhibit subtle, but important, differences with respect to analogous systems in full general relativity. Additionally, the role of a magnetic field in BNS mergers is also under study. Potentially, an organized postmerger field may play a crucial role in the generation of a jet were a binary to power a sGRB. Since it is generally expected that neutron stars have some magnetization, determining what electromagnetic effects could arise is important.

Here we explore the dynamics of binary neutron star systems with increased realism: we study stars described by different realistic equations of state; we consider the role of magnetization in the postmerger dynamics, and we account for neutrino cooling effects through a leakage algorithm. We estimate the luminosities for the emitted neutrinos with the leakage scheme and apply a more refined calculation, not generally applied to binary mergers, to find the average neutrino energies in an approach that takes into account redshifted neutrinos originating from the last points of scattering in the merged object. We confirm behavior recently observed in [34] for different equation of state (EOS) and present a detailed analysis of: the ejecta distribution, the full gravitational waveforms together with an analysis of their distinguishability, neutrino production and possible detectability using two different methods, and the role of magnetization. The increased realism of our simulations leads us to speculate that observations of kilonova and heavy element abundances in deep sea sediments suggests that a soft EOS describes the interior of neutron stars.

Details of our numerical implementation can be found in previous work [2,22,32,38,39]. We summarize details in Sec. II, present results in Sec. III, and discuss these results in Sec. IV. We defer to Appendices a description of the primitive solver and convergence tests.

II. NUMERICAL IMPLEMENTATION

Below we briefly summarize: (i) the evolution equations for the spacetime and the magnetized fluid; (ii) the prescriptions employed for the microphysical equations of state and the neutrino cooling scheme; and (iii) a description of the quantities employed to analyze the dynamics. Full details of our implementation are described in [32]. We adopt geometrized units where $G = c = M_\odot = 1$, although some results are reported more naturally in physical cgs units.

A. Evolution equations

The Einstein equations in the presence of both matter and radiation can be written as

$$G_{ab} = 8\pi(T_{ab} + \mathcal{R}_{ab}), \tag{1}$$

where G_{ab} is the Einstein tensor, $\mathcal{R}_{ab}$ is the contribution from the radiation field, and T_{ab} is the stress energy tensor of a magnetized, perfect fluid.

We solve the Einstein equations by adopting a $3+1$ decomposition in terms of a spacelike foliation. The hypersurfaces that constitute this foliation are labeled by a time coordinate t with unit normal n^a and endowed with spatial coordinates x^i. We write the spacetime metric as

$$ds^2 = -\alpha^2 dt^2 + \gamma_{ij}(dx^i + \beta^i dt)(dx^j + \beta^j dt), \tag{2}$$

with α the lapse function, β^i the shift vector and γ_{ij} the metric on spatial hypersurfaces. We write the Einstein equations in terms of the BSSN-NOK formalism [40–43], supplemented with appropriate gauge conditions; the "$1+\log$" slicing and the Γ-driver shift conditions, as detailed in [32]. In the problem of interest, radiation energies and stresses are much smaller than matter energies, or $|\mathcal{R}^{ab}| \ll |T^{ab}|$. This observation, together with the fact that a neutrino leakage scheme cannot possibly treat the radiation stress tensor completely consistently, allows us to ignore $\mathcal{R}_{ab}$ as a source term for the Einstein equations.

We model the matter as a magnetized perfect fluid with a stress energy tensor T_{ab} given by

$$T_{ab} = h u_a u_b + P g_{ab} + F_{ac}F^c_b - \frac{1}{4} g_{ab} F_{cd} F^{cd}, \tag{3}$$

where h is the fluid's *total* enthalpy $h \equiv \rho(1+\epsilon) + P$, and $\{\rho, \epsilon, Y_e, u^a, P\}$ are the rest mass energy density, specific internal energy, electron fraction (describing the relative abundance of electrons compared to the total number of baryons), four-velocity, and pressure of the fluid, respectively. Magnetic effects are included in the Faraday tensor, F_{ab}, where a factor $1/\sqrt{4\pi}$ has been absorbed in its definition. Given an equation of state $P = P(\rho, \epsilon, Y_e)$ and a relativistic Ohm's law, the equations determining the magnetized matter dynamics are obtained from conservation laws. We adopt the ideal magnetohydrodynamics (MHD) approximation, which states that the fluid is described by an isotropic Ohm's law with perfect

conductivity so that the electric field vanishes in the fluid's frame $F_{ab}u^b = 0$, because it provides a simple, yet realistic, model that keeps the number of fields needed to describe the electromagnetic effects to a minimum (in contrast to, say, a resistive MHD approach [44,45]).

The equations of motion consist of the following conservation laws:

$$\nabla_a T^a_b = \mathcal{G}_b, \tag{4}$$

$$\nabla^a (T_{ab} n^b) = 0, \tag{5}$$

$$\nabla_a (Y_e \rho u^a) = \rho R_Y, \tag{6}$$

$$\nabla_a {}^* F^{ab} = 0. \tag{7}$$

The sources $\mathcal{G}_a$ ($\equiv -\nabla_c \mathcal{R}^c_a$) and R_Y are the radiation four-force density and lepton sources which are determined within the leakage scheme. These equations are conservation laws for the stress-energy tensor, matter, lepton number, and Maxwell tensor, respectively. Notice that, in the absence of lepton source terms ($R_Y = 0$), Eq. (6) becomes a conservation law for leptons, similar to the baryon conservation law, i.e., Y_e is a mass scalar. These conservation equations combined with the Einstein equations, Eq. (1), comprise the complete set of equations we employ to describe the systems of interest.

The matter equations of motion in Eqs. (4)–(7) are written in balance law form

$$\partial_t \mathbf{u} + \partial_i \mathbf{f}^i(\mathbf{u}) = \mathbf{s}(\mathbf{u}) \tag{8}$$

by defining a set of *conservative* variables $\mathbf{u}$. The primitive (or physical) quantities are recovered from the conservative ones by solving a system of nonlinear equations, described in detail in Appendix A. Due to the inability of current fluid codes to evolve very rarefied matter, we impose a floor on the density, so that a tenuous atmosphere fills the domain outside the stars with constant density of 6×10^5 g/cm^3.

We use finite difference techniques on a regular, Cartesian grid to discretize the system [46,47]. The geometric fields are discretized using a fourth order accurate scheme satisfying the summation by parts rule, while a high-resolution shock-capturing method based on the Harten-Lax-van Leer-Einfeldt flux formula with piecewise parabolic method reconstruction are used to discretize the fluid and the electromagnetic variables. The fluid equations are written in a finite difference discretization (rather than finite volume) as prescribed for the third-order essentially non-oscillatory method [38,48], which simplifies coupling the fluid equations to the Einstein equations. The time evolution of the resulting equations is performed by using a third order accurate Runge-Kutta scheme [38,49]. To ensure sufficient resolution is available in an efficient manner, we employ adaptive mesh refinement (AMR) via the HAD computational infrastructure that provides distributed, Berger-Oliger style AMR [50,51] with full subcycling in time, together with an improved treatment of artificial boundaries [52].

B. Equations of state and neutrino transport

We use finite-temperature equations of state based on several relativistic mean field models of the nuclear interaction to model both neutron star matter and the hot, lower density material present during and after the merger. These different nuclear interactions give different cold neutron star structures and correspondingly different neutron radii and maximum masses. The use of a microphysical EOS over a simple polytrope is also needed to model neutrino interactions as the neutrino emission, absorption, and scattering rates depend sensitively on the matter density, temperature and composition. We use publicly available EOS tables [53] described in [54]. We have rewritten some of the library routines for searching the table to make them faster and more robust. These routines will be available on the HAD webpage [50].

The leakage scheme seeks to account for (1) changes to the (electron) lepton number and (2) the loss of energy from the emission of neutrinos. Because the dynamical time scale for the postmerger is relatively short, radiation momentum transport and diffusion are expected to be subleading effects. As is standard, we consider three species of neutrinos: ν_e for electron neutrinos, $\bar{\nu_e}$ for electron antineutrinos, and ν_x for both tau and muon neutrinos and their respective antineutrinos. Our scheme is based on the open-source neutrino leakage scheme from Ref. [54], also available at [53]. In particular, the leakage scheme provides the fluid rest frame energy sink $\mathcal{Q}$ and lepton sink/source R_Y due to neutrino processes. R_Y is the source term for a scalar quantity and therefore is the same in all frames. We express the source term for the energy and momentum in an arbitrary frame as

$$\mathcal{G}_a = \mathcal{Q} u_a. \tag{9}$$

Since the effect of neutrino pressure is small [55] and difficult to accurately capture with a neutrino leakage scheme, we ignore its contribution in the fluid rest frame. As mentioned, the details of our implementation can be found in Ref. [32], which also describes a novel and efficient calculation of the optical depth.

C. Analysis

We compute several quantities to analyze the quality of the solution as well as the dynamics and main characteristics of the system. A useful quantity to assess the correctness of the numerical solution is the total baryonic mass in the domain

$$M_b = \int \rho W \sqrt{\gamma} dx^3, \tag{10}$$

where W is the Lorentz factor. Because this mass should remain constant, we monitor it and also study its convergence in Appendix B.

Among the three possible signals produced by a BNS, the cleanest signal is provided by gravitational waves, which are potentially observable by the upcoming aLIGO/VIRGO to a distance of ≈450 Mpc. We extract this signal from our simulations by computing the Newman-Penrose scalar Ψ_4, which is directly related to the metric perturbation components by $\Psi_4 = \ddot{h}_+ - i\ddot{h}_x$ in the appropriate Bondi frame [56,57] (cf. [58]). We compute Ψ_4 on several spheres centered on the origin and with radii of $\{225, 300, 375\}$ km, i.e., far from the sources, in the wave zone. Performing the calculation on multiple spheres allows various consistency checks to confirm the validity of the signal. As is customary, we expand Ψ_4 in terms of spin-weighted spherical harmonics (with spin weight $s = -2$)

$$r\Psi_4(t, r, \theta, \phi) = \sum_{l,m} \Psi_4^{l,m}(t, r)^{-2}Y_{l,m}(\theta, \phi). \tag{11}$$

We also extract the instantaneous GW angular frequency from the primary ($l = m = 2$) mode through the relation

$$\omega = -\frac{1}{2}\mathrm{Im}\left[\frac{\dot{\Psi}_4^{2,2}}{\Psi_4^{2,2}}\right]. \tag{12}$$

The high cost of BNS simulations makes computing the full waveform relevant for matched-filtering analysis for data obtained by detectors such as aLIGO/VIRGO in full relativity impractical. However, for larger separations (low frequencies), post-Newtonian (PN) analyses provide excellent approximations. Therefore, our simulations concentrate primarily on the merger stage, and hybrid waveforms are constructed by matching the simulation waveforms to PN waveforms. Among the available PN waveforms, the Taylor-T4 approximation has proven quite convenient for binary black hole systems [59], and has recently been expanded to account for tidal effects [60] (cf. [61]). Our simulations span the last 4–6 orbits (depending on the EOS) and can be matched to the PN waveforms (by suitably blending over a cycle) to construct a complete waveform within aLIGO's frequency window. This allows us to calculate the gravitational wave power as a function of frequency and contrast it with the expected noise curve of aLIGO.

Another possible signal is provided by neutrinos produced by the shock-heated material during merger and afterward. Provided the event takes place relatively nearby, such neutrinos would be observable in current detectors such as Super-Kamiokande [62] and IceCube [63] as well as future detectors such as Hyper-Kamiokande [64]. We extract the neutrino luminosity and compute from it the distance at which a detection could take place.

Electromagnetic signals are also possible and would provide complementary information about the system (and with the possibility of covering a much wider set of frequencies due to the mature stage of detectors in the electromagnetic band). To extract such information, reasonable models connecting possible observations with particular characteristics of the systems are required. The details of such models generally rely on different assumptions and, in many cases, involve longer time scales than those that can be reasonably probed within a full general relativity simulation. However, one can explore the level to which consistent conditions are provided for such schemes. In particular, the lifetime of the MNS, the time scale for possible black hole formation, and the characteristics of any material outflow are key physical parameters (see e.g. [30,65–67] and references cited therein). Thus, we monitor the behavior of the formed MNS—e.g. central density and multipolar structure—as well as the properties of matter within our simulations, supplemented with reasonable approximations to connect with possible phenomena at longer time scales.

We assess the dynamics of all stellar material, at some representative times after the merger, by assuming it moves along geodesics. We compute its specific energy (as measured at infinity) ($\tilde{E} \equiv -u_t - 1$) and consider the material unbound if $\tilde{E} > 0$. We then produce histograms displaying various quantities which characterize the state of the bound and unbound material for the different EOS. In particular, to generate a histogram characterizing some quantity x (e.g. temperature), we compute a series of histogram heights, h_i, for bins extending from $b_i \to b_{i+1}$ (e.g. 10 to 20 MeV) as an integral over the whole space $h_i = \int \Theta(x - b_i)\Theta(b_{i+1} - x)\rho dV$, where $\Theta(x)$ is the Heaviside function. Although one may initially expect that one must loop over the grid for every bin, in practice a single sweep over the domain suffices because, at each gridpoint, the integrand gets added to just one bin.

III. NUMERICAL RESULTS

We concentrate on equal-mass binaries with individual gravitational masses given by $1.35M_\odot$, a value consistent with current observations [68]. We consider three distinct microphysical EOS: SFHo [69], DD2 [70] and NL3 [70]. These three EOS produce cold neutron stars whose radii cover a large range of values. In particular, the SFHo EOS gives the smallest radii (≈12 km for a mass of $1.35M_\odot$) among the three and is therefore considered a *soft* EOS. The NL3 EOS yields a large radius (≈15 km for the same mass) and is considered *stiff*. The DD2 EOS leads to an intermediate radius (≈13 km). We display the gravitational mass of isolated neutron stars for each EOS in Fig. 1.

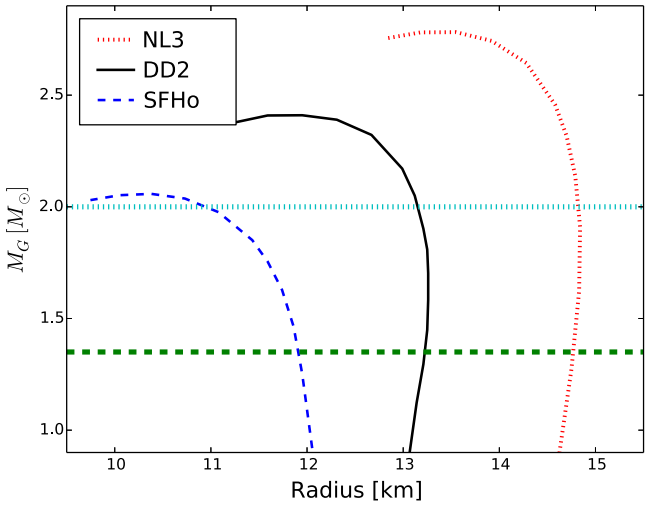

FIG. 1 (color online). Gravitational mass as a function of the circumferential radius for the three different microphysical EOS considered here. The horizontal, light blue line shows the maximum mass astrophysically measured for a neutron star [71,72] and the horizontal, green line indicates the mass considered in this paper. These curves were generated with the MAGSTAR solver, part of the LORENEpackage [73].

A horizontal, green line at $1.35M_\odot$ shows the stars considered here and its intersection with the three curves indicates the three different radii. All three EOS can produce neutron stars with a mass of at least $2M_\odot$, consistent with neutron star mass observations [71,72].

We concentrate on the late stages of the coalescence, roughly the last 4–6 orbits (depending on EOS), of equal mass, irrotational binary neutron stars. The physical parameters of the binaries and our grid setup are summarized in Table I. To monitor convergence of the solutions, we evolved the binary described by the DD2 EOS with three different resolutions obtaining convergent results (see Appendix B). For the two other EOS, we evolved only two different resolutions confirming that the differences between the two were consistent with those of the DD2 case. (For reference, unless otherwise specified, we set $t = 0$ as the time when all binaries are separated by 45 km.)

As mentioned, we include the effects of neutrino cooling and magnetic field in the dynamics. To reduce the significant computational overhead that these introduce, neutrino cooling is not calculated until a few milliseconds before merger when matter heats up and neutrino effects become significant. Likewise, we give the stars a poloidal magnetic field (with maximum strength 10^{13} G) a few milliseconds prior to merger. This strategy allows us to consider both the role of neutrino production and stellar magnetization in an efficient manner because neither cooling (the stars are cold prior to merger) nor magnetic field effects [22,74] affect the dynamics prior to merger.

A. Gravitational waves

At large separations, all binaries follow the same trajectory since the internal structure of the binary constituents only contributes at fifth PN order (see e.g. [75]). However, as the binary tightens, differences from a point-particle approximation arise and increase as the merger ensues. Such differences are intrinsically related to the tidal deformability of the stars which is, in turn, directly tied to the EOS.

We summarize the premerger dynamics of our three binaries in Fig. 2. The (coordinate) separation, the GW signal Ψ_4 ($l = 2, m = 2$ component), and the instantaneous GW frequency, all as functions of time, are shown. Also included in the bottom frame is the gravitational wave frequency as predicted by the T4 PN approximation [59]. During the first eight milliseconds, all the binaries agree with each other and with the T4 approximation. Only at times closer to merger do the binaries begin to differentiate from each other and from the point-particle approximation.

The first EOS to show differences is NL3, followed by DD2, and then SFHo. This is the expected behavior as the NL3 EOS corresponds to the largest neutron star radii, DD2 the intermediate and SFHo the smallest radii. Tidal effects are proportional to k_2R^5 (where k_2 is the tidal Love number and R is the stellar radius), and therefore, for fixed mass, differences in radii are dominant. We take advantage of this early agreement to compute a complete wave train by creating a hybrid of the PN and our simulated waveforms which we show in Fig. 6 and discuss later. Of course, the

TABLE I. Summary of the parameters of the binary systems considered in this paper. The initial data were computed using the BIN STAR solver from the LORENE package [73], by imposing beta equilibrium and a constant temperature $T = 0.02$ MeV. All the binaries start from an initial separation of 45 km and the outer boundary is located at 750 km: the ADM mass $M_0^{\rm ADM}$ and angular momentum $J_0^{\rm ADM}$ of the system, the baryon mass of each star $m_b^{(i)}$ and its coordinate radius $r^{(i)}$, the initial orbital angular frequency Ω_0 of the system, the initial GW frequency $f_0^{\rm GW} \equiv \Omega_0/\pi$ and the best resolution $\Delta x_{\rm min}$ covering both the stars. For the DD2 EOS, higher and lower resolutions were carried out for the study of convergence (see Appendix B).

EOS	$M_0^{\rm ADM}[M_\odot]$	$J_0^{\rm ADM}[GM_\odot^2/c]$	$m_b^{(i)}[M_\odot]$	$r^{(i)}$ [km]	Ω_0 [rad/s]	$f_0^{\rm GW}$ [Hz]	$M_{\rm eject}[M_\odot]$	$\Delta x_{\rm min}$ [m]
NL3	2.7	7.40	1.470	12.63	1778	566	1.6×10^{-6}	230
DD2	2.7	7.39	1.485	10.88	1776	565	4.3×10^{-4}	230 (275 and 192)
SFHo	2.7	7.38	1.498	9.47	1775	565	3.2×10^{-3}	230

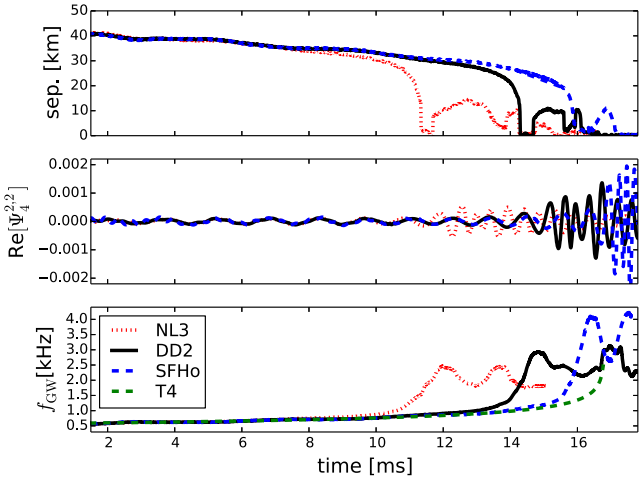

FIG. 2 (color online). Orbital parameters displayed as a function of time for the three different EOS considered here. (Top) Separation between the stars, computed as the coordinate distance between the maximums of the density. (Middle) Primary gravitational wave mode $l = m = 2$. (Bottom) The frequency of the primary GW mode where $f_{GW} = \omega/(2\pi)$ [see Eq. (12)]. Also shown is the frequency obtained from the Taylor T4 approximation. Note that differences among the EOS only appear at times near merger.

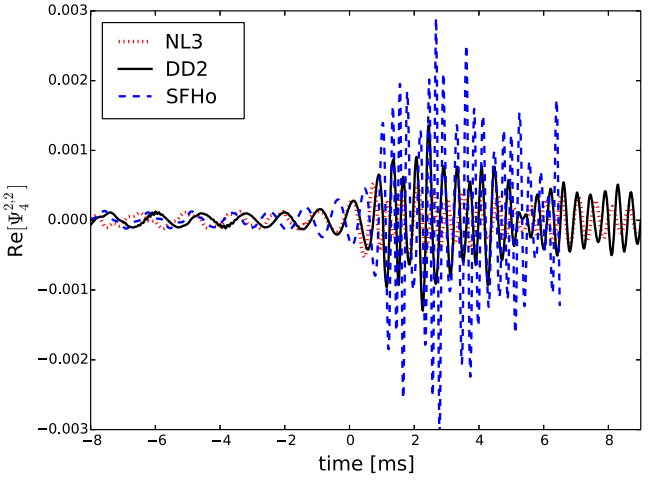

FIG. 3 (color online). Comparison of the near-merger behavior of the GW signal, as indicated by the primary mode of Ψ_4. The different signals have been shifted in time such that $t = 0$ corresponds to the time when the separation between the density maximums vanishes. The significant differences among the signals near merger indicate that information about the internal stellar structure (e.g. details of the EOS, radius, compactness) is encoded within the gravitational wave signature.

merger itself is highly nonlinear, and so an examination of the merger waveforms does not involve any further comparison with PN results.

Considering now the merger, we shift times in each case such that $t = 0$ refers to the moment when the maximum density first occurs at the origin of the binary. Figure 3 presents the gravitational waveforms with time measured from the merger. Note that all three signals prior to merger (negative times) oscillate within a common amplitude envelope. This behavior can be understood with an effective, and approximate, one-body problem point of view. In such a problem, the central object has a mass approximately given by the total mass of the system and radiative properties can be captured by the infall of a particle of reduced mass $\mu = m_1 m_2/(m_1 + m_2)$. Shifting time so that all cases merge at $t = 0$ allows for identifying a natural common time, and phase differences are a consequence of the particle being released at different times with respect to the shifted time. Such an approach has been at the core of a number of effective prescriptions for capturing various aspects of the two-body problem in general relativity (e.g. [76–79]).

Figure 3 also allows for a clear comparison of the strength of the gravitational waves and the waveform periods. The SFHo EOS achieves the largest amplitude during merger as a natural consequence of yielding the smallest stellar radii. A smaller radius means that the merger takes place deeper in the gravitational potential of the binary, and hence more energy is released, resulting in a more dynamical and violent collision. In contrast, the weakest peak signal with longest period is produced by the NL3 EOS with its large radii while the DD2 binary is intermediate between the two extremes considered.

Qualitatively, the mergers for all three EOS proceed similarly. The stellar orbit tightens as GW are emitted, and, as the stars get closer, tidal deformations grow. Evidence for such deformations can be appreciated, for the DD2 case, in the first two frames of Fig. 4. (We caution however that coordinate effects are not taken into account in the figure; observable effects of tidal deformations are better represented in the gravitational waveforms obtained.) After the merger, strong radial oscillations in the remnant lead to peak densities bouncing outward (with respect to the corotating frame), as shown in the last four frames of Fig. 4. These bounces are also apparent in the separation plot in Fig. 2. The oscillations however are stronger—larger in amplitude and longer lasting—as the EOS becomes stiffer, with mergers at earlier times and smaller angular velocities (as can be appreciated in Figs. 2 and 3).

The resulting hot MNS will cool down as well as lose energy and angular momentum via emission of neutrinos and gravitational waves. Furthermore, its velocity distribution will be redistributed through angular momentum transport by hydrodynamical and electromagnetic effects. Collapse to a black hole will eventually take place if the mass of the MNS is higher than the maximum allowed mass for a given EOS. Inspection of Fig. 1, together with the observation that the amount of unbound mass is relatively small in all cases, indicates that at least the SFHo case is expected to collapse to a black hole at some

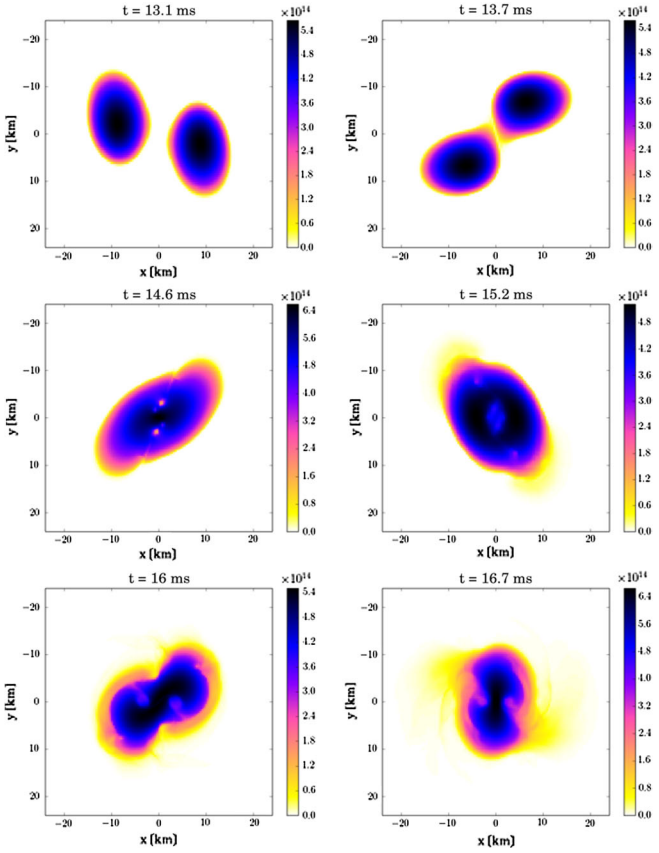

FIG. 4 (color online). Density on the equatorial plane for the DD2 EOS. The stars merge at $t \approx 14.3$ ms. The first two frames show the system premerger as tidal deformations arise. Also visible in the final four frames is the rebound of the stellar material postmerger.

point (see also [19,34]). Such an expectation arises naturally because the maximum mass allowed with this EOS for a nonrotating star is $\approx 2.05 M_\odot$, and, while rotation helps increase the maximum allowable mass, it cannot do so beyond ≈20% [80]. Indeed, for the times studied in this work, the SFHo binary collapses to a black hole ≈7 ms after merger.

Additional information about the properties of the neutron star are provided by the GW after the merger. Figure 5 displays the power spectral density of the Fourier transform for the main GW mode at this stage. The spectrum shows several characteristic peaks. The dominant peak (the one with the most power), $f_{\rm peak}$, is associated with the rotational behavior and quadrupolar structure of the MNS. As mentioned, a softer EOS results in a merger at higher frequency as the smaller radius stars coalesce. This effect is apparent when comparing the spectra for the different EOS in Fig. 5. The peak frequencies are also presented in Table II.

Beyond this qualitative discussion, the peak frequency is slightly higher than twice the orbital frequency at the time of merger. Since there will be further compression of the

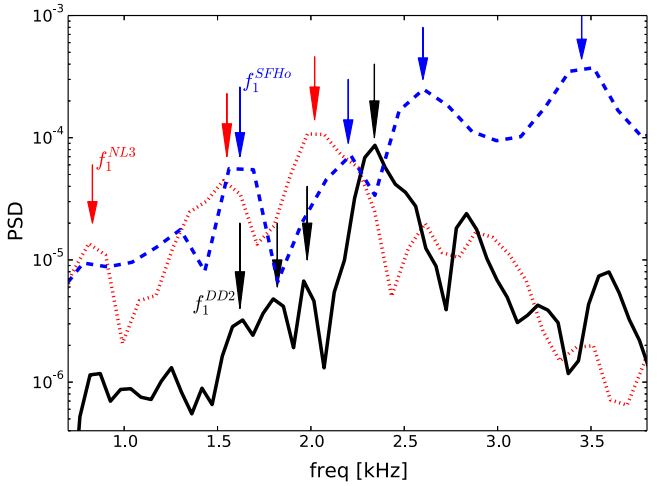

FIG. 5 (color online). Power spectral densities (PSD) of the gravitational waveforms after the merger. The Fourier transforms display the main oscillation modes of the MNS. The arrows indicate particular peaks with their corresponding frequencies f_i presented in Table II.

merged MNS, its rotational frequency will be higher than the frequency estimated by Kepler's law at the moment of contact. Nevertheless, the Keplerian orbital frequency can be used to estimate $f_{\rm peak}$ as [82]

$$f^i_{\rm peak}/f^j_{\rm peak} \approx (R_j/R_i)^{3/2}, \tag{13}$$

where i and j denote different binaries with stellar radii given by R_i and R_j, respectively. Interestingly, several other subdominant peaks exist at lower frequencies that arise from oscillations of the MNS. All these peaks offer interesting future detectability prospects for third generation detectors (aLIGO/VIRGO/KAGRA) that will have specifically tuned configurations to increase sensitivity in the higher frequency range or even signal-stacking possibilities (e.g. [83]).

Recently, Ref. [81] indicated that these low frequency, secondary modes can be traced to two different mechanisms, although this is still a matter of debate (see for instance [84,85]). Using the same naming conventions of [81], the first, secondary peak f_{2-0} corresponds to a nonlinear combination of the dominant quadrupolar mode with the quasiradial oscillations of the star. The other subdominant peak, $f_{\rm spiral}$, is produced by a strong spiral deformation induced at the merger time that lasts for just a few rotational periods. We calculate these frequencies for our simulations using the estimates in Ref. [81], which are based on the compactness of the neutron stars, and include these in Table II. Comparing the frequencies extracted from our simulations with the estimates, we find that the simulation values for both the dominant, f_1, and secondary, f_2, peaks are consistent with $f_{\rm peak}$ and $f_{\rm spiral}$, respectively. Also, the simulation frequencies $\{f_3, f_4\}$ are in reasonable

TABLE II. Postmerger oscillation frequencies in kHz. The frequencies of the various peaks of the postmerger GW spectrum (see Fig. 5) are shown as f_1, f_2, f_3, and f_4. The compactness of the neutron stars for each EOS (obtained from the initial data for an isolated star) along with the predicted peak frequencies from Ref. [81]. The decent agreement between f_1 and $f_{\rm peak}$, between f_2 and $f_{\rm spiral}$, and between either f_3 or f_4 with f_{2-0} suggests consistency with the model presented in [81].

EOS	f_1	f_2	f_3	f_4	M/R	$f_{\rm peak}$	$f_{\rm spiral}$	f_{2-0}
NL3	2.0	1.5	0.8		0.135	2.2	1.6	1.2
DD2	2.3	2.0	1.8	1.62	0.15	2.6	1.9	1.5
SFHo	3.4	2.6	2.2	1.6	0.167	3.2	2.4	2.1

agreement with f_{2-0} for the softest and intermediate EOS (SFHo and DD2).

Finally, we return to the complete gravitational wave train. As discussed, the early behavior is well approximated by the PN (Taylor T4) expansion which can be augmented to include leading order tidal effects [60,61]. We thus obtain a more complete waveform by matching this augmented PN signal at early times to our numerical signal before merger to form a hybrid waveform. (Further improvements into the early signal can be achieved, see e.g. [79], though such improvements would not affect the main conclusions drawn here.) The matching is accomplished by choosing a cycle after initial numerical transients but still well before merger. Within this cycle, a weighted average of the two waveforms is calculated using a tanh function that transitions from 0 to 1. We show (a portion of) the hybrid waveforms resulting from the three EOS in Fig. 6. For illustrative purposes, we also show a portion of the (real part of the $l = 2, m = 2$ component of) Ψ_4 for the two SFHo waveforms in Fig. 7.

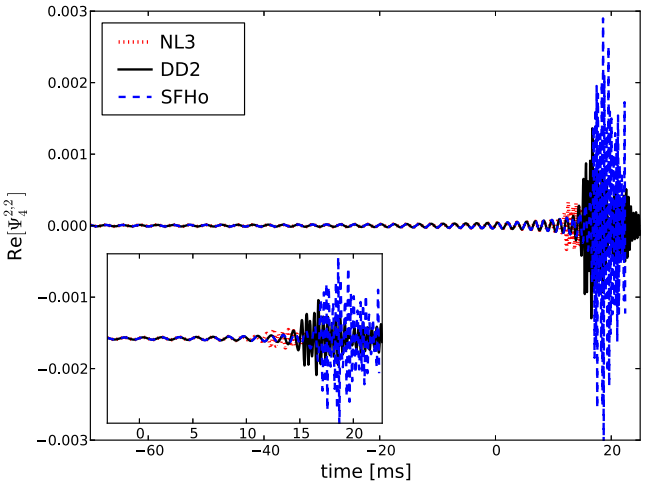

FIG. 6 (color online). Hybrid waveforms obtained by matching the PN waveform with the respective EOS waveform from the evolution of the binary. These waveforms are used for comparing signals with aLIGO noise curves in Fig. 8.

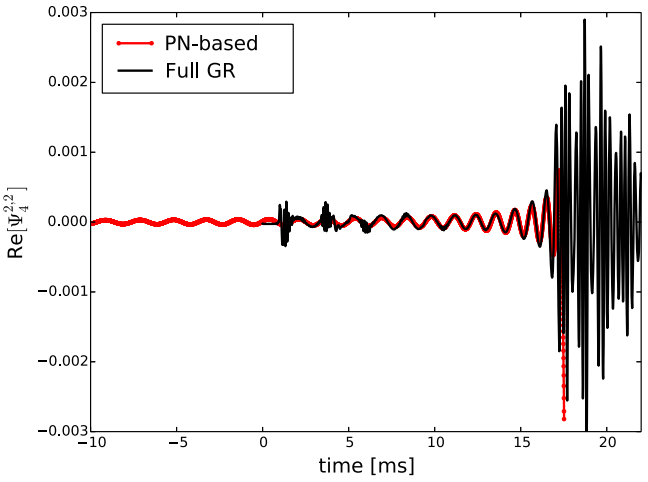

FIG. 7 (color online). Real part of the $l = 2, m = 2$ component of Ψ_4 for both the PN-based and numerical evolution waveforms for the SFHo EOS.

Additionally, we compare the strength of the signals to the expected noise curve of Advanced LIGO as illustrated in Fig. 8, which presents the Fourier spectrum of the GW (multiplied by $\sqrt{f}$) for binaries at 100 Mpc versus frequency together with two fits to the aLIGO noise curve (the so-called "no signal recycling mirror" and the "zero-detuned high-power case"). As mentioned, differences among the waveforms arise only at high frequencies when tidal effects become relevant. The NL3 waveform departs first from the other two cases because the larger stellar radii lead to stronger tidal effects. The differences among the three EOS arise below the aLIGO noise curve in the case without a signal recycling mirror but could be captured in

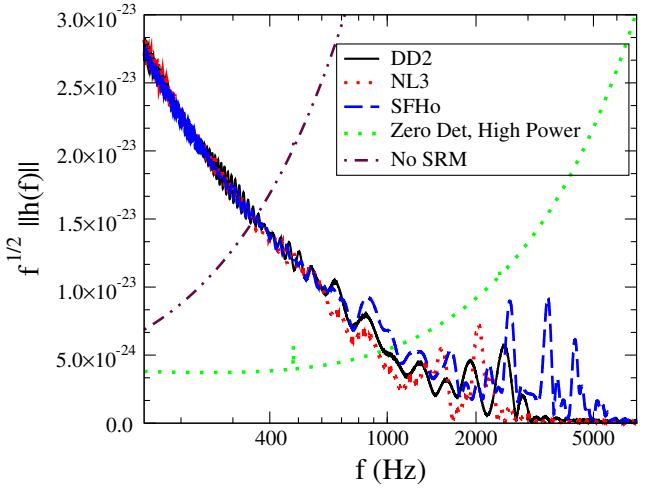

FIG. 8 (color online). Fourier spectrum of the GW signals for the three binaries. The dotted and dash-dotted monotonic curves at high frequencies show two fits to the noise power spectrum $\sqrt{S_h}$ of aLIGO [specifically the zero-detuned high-power and the no signal recycling mirror (NSRM) cases, see [86].

the "broadband" (zero-detuned, high power case) configuration.

Finally, we can compute the "distinguishability" between the different waveforms (as described in e.g. [33], see also [24,87,88]) using the "zero-detuned high-power case" noise curve in aLIGO. Without allowing for frequency shifts (and not normalizing our waveforms), we find the values for $\delta h = \sqrt{\langle h_i - h_j, h_i - h_j \rangle}$ are given by $\approx\{1.33, 1.36, 1.45\}$ when considering the pairs SFHo-DD2, SFHo-NL3 and DD2-NL3 respectively within the frequency window $f \in [300, 8000]$ Hz. Since all cases satisfy $\delta h > 1$ the gravitational waves will be distinguishable from each other by aLIGO with the zero-detuned high-power case configuration. In contrast, these values reduce to $\delta h \approx \{0.27, 0.28, 0.32\}$ for the no signal recycling mirror configuration.

B. Matter dynamics: Outflow and ejecta

Having presented characteristics of the GW produced mainly by the bulk motion of the stars, we now turn to an analysis of the material outflow resulting from the collision. While such motion leads only to subleading effects on the bulk dynamics (and hence on GW emission), the details of any outflow can be very important for producing electromagnetic and neutrino signals.

In particular, among the outflow, material bound to the system either remains part of the resulting MNS or otherwise contributes to an accretion disk which may potentially power a sGRB (see e.g. [89]). On long time scales, such a disk can induce winds that produce optical electromagnetic emission via the radioactive decay of r-process elements [13]. Furthermore, the fallback of bound material may trigger the eventual collapse of the remnant star to a black hole which, in turn, could power an intense burst of electromagnetic radiation [27,90].

Another particularly interesting mechanism powered by outflows is the proposed kilonova in which material ejected by the collision undergoes r-process nucleosynthesis. Being ejected from the core region, the behavior of this material and its consequences can be analyzed without worrying about the rather involved behavior of the central region. Indeed, as discussed in [10], a promising source of electromagnetic signals is the radioactive decay of r-process elements formed in the ejecta (see also, e.g. [12]). Such signals have specific characteristics observable on the order of days after the merger [14,15]. Importantly, such characteristics can have a rather tight dependence on the parameters of the binary and the EOS describing the neutron stars involved.

Given the importance of the outflow, in the following we compare the properties of both bound and unbound material among the three EOS.

We begin our analysis of the merger and postmerger by presenting snapshots of important quantities just a few milliseconds after merger. Figures 9 and 10 display the

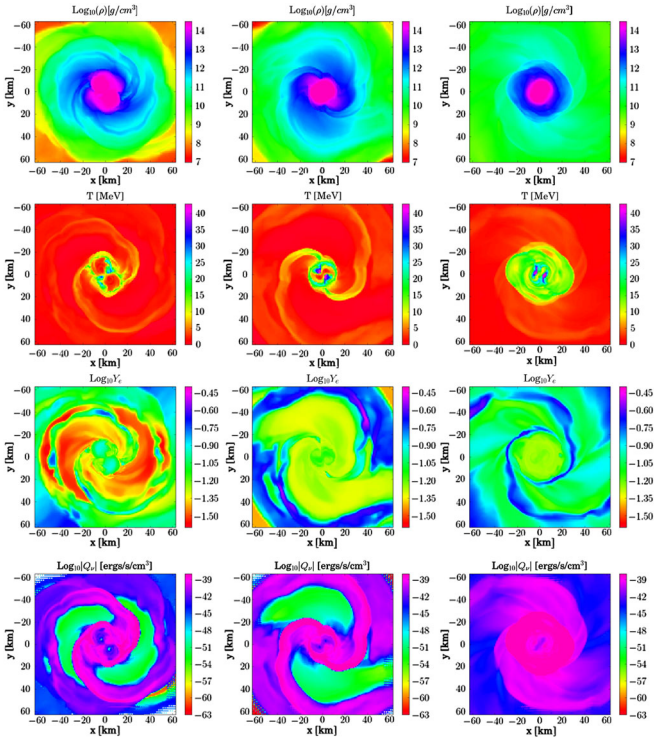

FIG. 9 (color online). Density, temperature, electron fraction and neutrino luminosity rate for the different EOS in the $z = 0$ plane at roughly $t = 3$ ms after the merger. Shown are the NL3 EOS (left), DD2 EOS (middle), and SFHo (right).

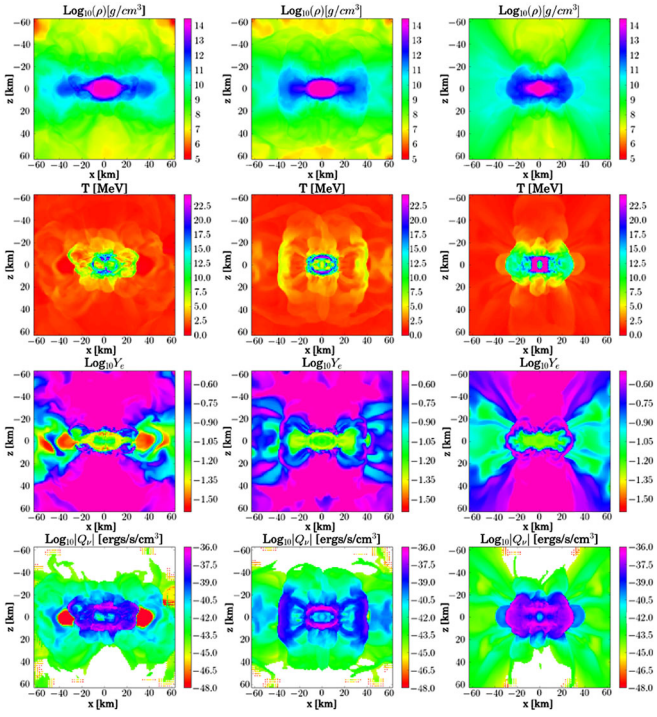

FIG. 10 (color online). Density, temperature, electron fraction, and neutrino luminosity rate for the different EOS in the $y = 0$ plane at roughly $t = 3$ ms after the merger. Shown are the NL3 EOS (left), DD2 EOS (middle), and SFHo (right).

density, temperature, electron-fraction, and neutrino luminosity along the $z = 0$ and $y = 0$ planes for the three EOS. The density snapshots show clear differences among the EOS, with the SFHo having a much more distributed, high density region than the NL3 remnant. This difference can be understood in terms of the stiffness of the EOS. In particular, the SFHo, being the softest of these EOS with the most compact stars, results in a more violent merger; the compact stars have further to travel to merge and have higher impact velocities. The violence serves to distribute the stellar material more than is seen with the stiffer EOS and, in particular, yields more ejecta. Likewise, the temperature of the material is generally higher for the softer EOS and, as a consequence, the neutrino production is also higher (we discuss further neutrino-related aspects in the next subsection).

To be more quantitative, we present a number of histograms that characterize the statistics of this postmerger material, measured at roughly $t = 3$ ms after the merger. We concentrate on the behavior of the matter at this early time to ensure that atmosphere effects do not contaminate the extracted values of the outflows. Note, however, that this implies that our quantities of unbound material might be consequently lower than the actual values, as matter can be ejected not only due to the tidal interactions, but also because of thermal pressure, which increases significantly at the merger due to shock heating. We present the velocity distribution in Fig. 11, as well as directional dependence (as measured with respect to the direction of the orbital angular momentum) in Fig. 12, the temperature in Fig. 13, and the electron fraction in Fig. 14. An important distinction is whether this material is bound to the remnant or whether it is unbound ejecta.

When looking at the unbound material, the reader should understand that the histograms display the fractional masses of material with some property. The huge disparity in unbound material among the EOS is therefore not immediately apparent. Therefore, for the unbound matter we include histograms of the absolute quantities in the

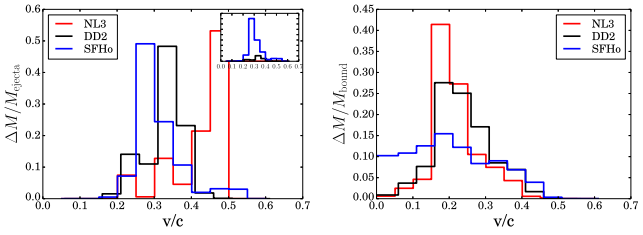

FIG. 11 (color online). Distributions of speeds for stellar material. (Left) The fraction of *ejected* mass binned according to velocity. The inset shows instead the absolute mass binned in the same way. The inset demonstrates that the NL3 case has essentially no unbound mass compared to either the DD2 or SFHo cases, and the SFHo has significantly more unbound mass than the DD2 case. (Right) The fraction of *bound* material with some particular velocity.

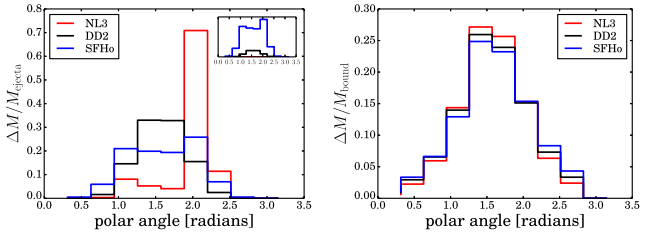

FIG. 12 (color online). Polar distributions of material for the different EOS cases. Stellar material is binned according to its polar angle. (Left) *Ejected* material. (Right) *Bound* material. Both bound and ejected material is mostly found near the orbital plane. The asymmetry across the orbital plane for the NL3 unbound mass is very pronounced and probably indicative roughly of our computational error because the amount of unbound material for that case is so small.

insets; the stiff EOS material is barely visible. In particular, SFHo has $0.0032M_{\odot}$ unbound material, the DD2 has roughly 13% of this amount and the NL3 has only 0.05% (these amounts are also included in Table I). That a soft EOS yields more ejecta agrees with recent results of Ref. [34], and correlates with the collision occurring deeper in the gravitational potential than for the stiffer EOS. The observation of an apparent kilonova [14,15], which would require significant ejecta, is therefore suggestive of a soft-intermediate EOS, provided the binary is composed of two neutron stars with similar masses. We will return to this point in the conclusion.

Figure 11 illustrates the fraction of ejected and bound mass, binned according to velocity. While the distribution in speeds of the bound material is within a similar range $v \in (0, 0.5)c$, although the velocities of the ejecta are quite different given the narrower peak for the stiffer equation of state. The stiffest EOS, NL3, has large velocities. It is not clear, however, if these high velocities have any physical significance because the quantity of ejecta is so tiny.

We display the polar angular distribution of the postmerger material in Fig. 12. The bound material is mostly in the equatorial plane, regardless of EOS. Unbound material is similarly distributed mostly near the equatorial plane. Both these observations imply the system avoids baryon poisoning along the polar regions and so winds could be

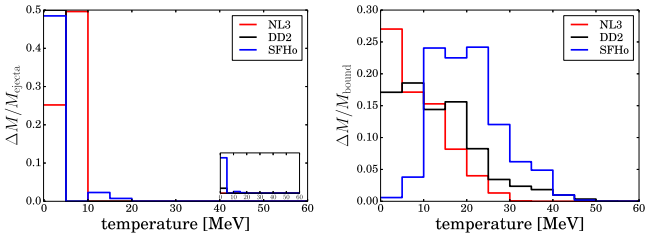

FIG. 13 (color online). Distributions in temperature of stellar material. (Left) Unbound material is generally cool for all three EOS. (Right) Bound material. The temperature of the SFHo case is noticeably higher than that of the stiff EOS.

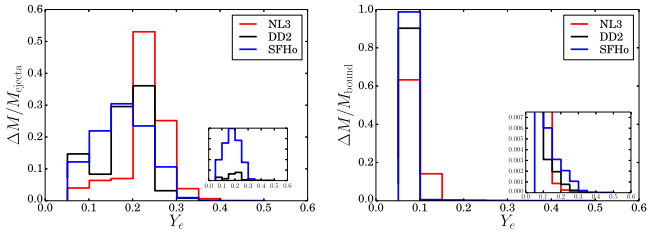

FIG. 14 (color online). Distributions of electron fraction for the stellar material. (Left) *Unbound* material for the different EOS. The inset shows the unrescaled amount of unbound material with the given electron fraction. Note that the outflow material is neutron rich ($Y_e < 0.3$). (Right) *Bound* material. The inset here does not show absolute quantities, but instead shows the same information as the main plot but with much smaller vertical scales.

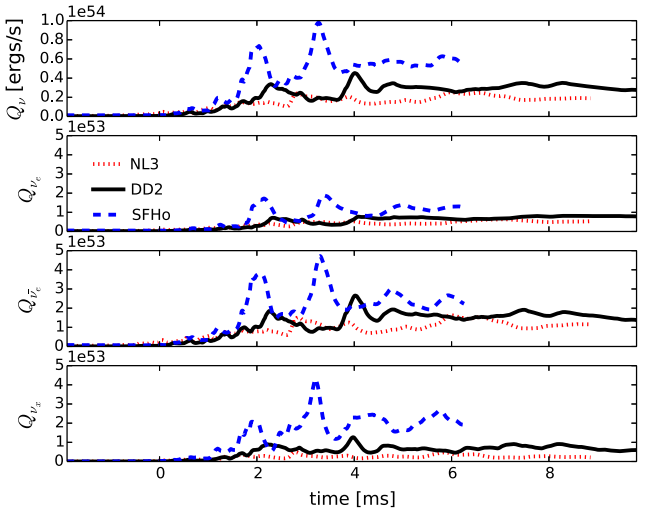

FIG. 15 (color online). Neutrino luminosities for the different EOS.

preferentially channeled along such regions. Such winds can also trigger the r-process although, as discussed below, for winds with electron fractions larger than about 0.2 [13,91], the signals from the radioactive decay would likely occur in the optical and ultraviolet bands instead of the infrared.

Figure 13 contrasts the temperature distribution among the EOS. The temperatures of unbound material are low for all three EOS. However, the bound material of the SFHo case is generally much hotter than the other two EOS [i.e., with a distribution peaked at temperatures in (10–20) MeV in the SFHo case as opposed to 0–5 MeV for the stiffer ones], as well as a tail with temperatures higher by 10 MeV with respect to the tail in temperatures measured for the DD2 and NL3 cases. As mentioned, the soft EOS yields a more violent collision with concomitant higher temperatures. The largest fraction of SFHo bound material is close to 30 MeV while the stiff peaks at roughly 10–20 MeV.

Finally, Fig. 14 shows the electron fraction distribution and, in particular, that the unbound material is generally quite neutron rich. The calculated values have a significant fraction below $Y_e \lesssim 0.22$, a rather robust condition for r-process nucleosynthesis being able to create high mass-number elements [13,92]. Consequently, an electromagnetic signal peaking in the infrared would be expected in such cases.

C. Neutrino emission

We compute neutrino cooling and the corresponding luminosity through a leakage scheme as reported in [32]. Figure 15 shows the luminosities for each neutrino species and the total neutrino luminosity as a function of time for each EOS. Following along the trend of the previous results which showed the largest gravitational wave emission and largest ejecta mass for the SFHo EOS, we also see the largest neutrino luminosity and, as discussed later, the largest neutrino average energy for this EOS. This reflects the fact that the temperature and decompressed mass achieved in this case is the highest. Irrespective of the particular EOS, it is evident that the luminosities for both electron neutrinos and electron antineutrinos become roughly comparable while the heavy-lepton neutrino types are less luminous (we note that the heavy lepton luminosity shown here is actually the contribution for all four heavy-lepton species). This dominance has already been observed in other binary neutron star mergers [18,32,93] and also neutron star–black hole mergers [55], and in simulations with more complete neutrino transport [34,94]. This phenomena is due to neutron rich material being shock heated and decompressed [95]. This neutron rich, low density, hot material is initially far below the new β-equilibrium value of Y_e and will preferentially emit electron antineutrinos until equilibrium is reestablished.

Given the high neutrino luminosities achieved during the merger it is interesting to study their possible detection in future and current facilities. For the purposes of detection on Earth, we are most interested in the spectrum and luminosity of the electron antineutrinos, as these neutrinos will produce the largest signal in Earth-based water Cherenkov detectors, such as the current Super-Kamiokande or IceCube detectors, or the future Hyper-Kamiokande detector. It is true that neutrino flavor oscillations can occur due to one or more of the following: (1) neutrino-neutrino interactions, (2) neutrino-matter interactions, or (3) oscillations in vacuum. In these cases, some fraction of the electron antineutrino spectrum will oscillate into heavy lepton antineutrinos and vice versa. The precise influence of neutrino oscillations on the electron antineutrino spectrum observed in Earth based detectors is unknown, but depends sensitively on the unknown neutrino mass hierarchy and the neutrino and matter conditions in the merger remnant [96]. For this reason, in our analysis we neglect oscillations and assume the electron antineutrino signal at Earth is the emitted signal from our merger calculation with a gravitational redshift.

We note that Ref. [94] recently showed that the electron antineutrino luminosity predicted from their leakage scheme, which is similar in design to ours, matches the prediction from a more complete neutrino transport calculation to better than ∼30%. Furthermore, the neutrino luminosities shown in Fig. 15 agree well with the recent results of [34], who study similar EOS and initial conditions. The leakage scheme also predicts a lepton loss rate that, in theory, provides an average energy for the emitted neutrinos. However, this average energy prediction is typically too high because it includes contributions from very high energy neutrinos leaking out from optically thick zones. In reality these neutrinos thermalize as they diffuse out. A more representative average energy is one determined by the thermodynamic conditions near the neutrinosphere, the location where the neutrinos leave thermodynamic equilibrium with the matter.

To make a more accurate determination of this neutrino average energy, we use the formalism described in Ref. [97]. We chose to examine the disk as seen by an observer looking down from $z = +\infty$, i.e. looking face-on towards the disk. To locate the neutrinosphere of the remnant disks for this direction, rays are traced down onto the disk from $z = +\infty$ and halted when the integrated optical depth reaches $2/3$. We repeat this for many (x, y) pairs. We ignore general relativistic effects on the ray propagation. The stopping location sets the neutrinosphere surface, $\mathcal{S}$. During the integration, at a given spatial location, we assume the opacity is the average over a Fermi-Dirac, zero chemical potential neutrino number distribution with a temperature equal to the local matter temperature. As contributions to the opacity we include: (1) elastic scattering of all neutrino species on neutrons, protons, and electrons; (2) neutrino capture on protons (neutrons) for electron antineutrinos (electron neutrinos); and (3) neutrino-antineutrino annihilation. As we include scattering cross sections, our neutrino surfaces correspond to the surface of last scattering, not necessarily the surface where the neutrinos thermodynamically decouple. The differences between these two surfaces is small for electron-type neutrinos and antineutrinos because the cross sections are dominated by the charged current processes, but this difference is larger for the heavy lepton neutrinos which do not have such interactions in BNS merger remnants. That being said, to determine the average energy of neutrinos emitted in this direction, for a particular neutrino species, we average over $\mathcal{S}$, and compute

$$\langle E_{\nu_i} \rangle = \int_{\mathcal{S}} dA \int dE E \phi_{\nu_i}(E, \mathcal{S}) \Big/ \int_{\mathcal{S}} dA \int dE \phi_{\nu_i}(E, \mathcal{S}), \tag{14}$$

where the integral is carried out over the neutrinosphere surface $\mathcal{S}$, determined by the rays; the Fermi-Dirac flux, $\phi(E, \mathcal{S})$, is given by

$$\phi(E, \mathcal{S}) = \frac{c}{2\pi^2 (\hbar c)^3} E^2 f_{\rm FD}, \tag{15}$$

where $f_{\rm FD}$ is the Fermi-Dirac distribution with a temperature equal to the local matter temperature on the surface $\mathcal{S}$. The neutrino energy will be gravitationally redshifted as neutrinos stream away from the merger remnant. We estimate the neutrino energy at infinity by transforming the emitted quantities using the invariance of phase-space density,

$$\frac{1}{c^2} \frac{dN}{d^3 x d^3 p} = \frac{f_{\rm FD}}{h^3 c^2} = \frac{I}{E^3}, \tag{16}$$

where I is the specific intensity, N the number of neutrinos leaving the source, and

$$\frac{dN}{d^3 x d^3 p} = \frac{c^2}{E^2} \frac{dN}{dA dt dE d\Omega}. \tag{17}$$

To proceed, let us denote the quantities measured by an observer with a "tilde" (i.e. the observed energy is $\tilde{E}$, the area differential is $d\tilde{A}$, etc.) while the analogous emitted quantities are E and dA, etc. Now, by invariance of I/E^3 we have

$$\frac{1}{c^2} \frac{dN}{d^3 \tilde{x} d^3 \tilde{p}} = \frac{1}{c^2} \frac{dN}{d^3 x d^3 p}. \tag{18}$$

Focusing on the left-hand side,

$$\frac{1}{c^2} \frac{dN}{d^3 \tilde{x} d^3 \tilde{p}} = \frac{1}{\tilde{E}^2} \frac{dN}{d\tilde{E} d\tilde{A} d\tilde{t} d\tilde{\Omega}} = \frac{f_{\rm FD}}{h^3 c^2}, \tag{19}$$

we obtain

$$\frac{dN}{d\tilde{t}} = \int \frac{f_{\rm FD}}{h^3 c^2} \tilde{E}^2 d\tilde{E} d\tilde{A} d\tilde{\Omega}. \tag{20}$$

We can now rewrite Eq. (20) in terms of the emitted quantities given that $\tilde{E} = \sqrt{g_{00}} E$, assuming that the emission is isotropic, and that distances are stretched by a factor of $(1 - r_s/r)^{-1/2} = g_{00}^{-1/2}$ (utilizing the Schwarzschild metric for simplicity). Thus, Eq. (20) can be reexpressed as

$$\frac{dN}{d\tilde{t}} = 4\pi \int \frac{f_{\rm FD}}{h^3 c^2} g_{00}^{3/2} E^2 dE \frac{dA}{g_{00}} = 4\pi \int \frac{f_{\rm FD}}{h^3 c^2} g_{00}^{1/2} E^2 dE dA, \tag{21}$$

and thus

$$\frac{dN}{d\tilde{t}} = \int g_{00}^{1/2} \phi(E, \mathcal{S}) dE dA. \tag{22}$$

We can proceed in a similar way for $\tilde{E} dN/d\tilde{t} = d\tilde{E}/d\tilde{t}$, and find

$$\frac{d\tilde{E}}{d\tilde{t}} = \int \frac{4\pi}{h^3c^2} g_{00} \frac{E^3}{e^{E/T}+1} dEdA = \int g_{00}\phi(E,\mathcal{S})EdEdA. \tag{23}$$

This agrees with the well-known result that the luminosity at infinity is $L_\infty = g_{00}L$ in the case where the neutrino surface is at a constant redshift.

Equation (23) contains g_{00} which must be evaluated at the neutrino surface. Then the average observed energy is $\langle E_{\nu_i}\rangle = (d\tilde{E}/d\tilde{t})/(dN/d\tilde{t})$. For simplicity, when evaluating the numerical value of g_{00}, we employ the Schwarzschild metric (in Schwarzschild coordinates) with a central black hole mass of $2.7M_\odot$. Inside 25 km (~3 Schwarzschild radii), to avoid spuriously overestimating the amount of redshift, we fix the value of the metric to the value at 25 km, i.e. $|g_{00}|(r < 25\ \text{km}) \sim 0.68$. (For the purpose of our estimates, this simple evaluation does not depend sensitively on these details however.) We present the average energies computed this way for several times and EOS in Table III. The SFHo merger emits the highest average neutrino energy, consistent with the highest matter temperatures achieved during the merger.

In Fig. 16, we show snapshots of the spatial distribution of the temperature at the neutrinosphere at ≈2.5–3 ms after merger for the three EOS and for each electron-type neutrino species. As the matter is primarily neutron rich, the electron neutrino neutrinosphere has a larger extent than the electron antineutrinosphere. The SFHo merger produces the most decompressed material and ejecta and the highest temperatures; thus powering the largest neutrino luminosity. This EOS also has larger and generally hotter neutrinospheres for all species. For the NL3 and DD2 EOS, the neutrinosphere is generally confined to the MNS except for the region around the tidal tails. These tails are cold and have little mass (see Sec. III B).

Armed with the neutrino luminosities and average energies, we can estimate the detection rate at Earth-based neutrino detectors. Given the uncertainties introduced by the leakage scheme, we make the following assumptions:

TABLE III. Observed (emitted, with no gravitational redshift taken into account in parentheses) neutrino average energies for electron antineutrinos and electron neutrinos, the electron antineutrino luminosity predicted from the leakage scheme (from Fig. 15), and the estimated instantaneous detection rate in Super-Kamiokande for a merger at 10 kpc from Earth via Eq. (25) for two different times and three EOS. In the text, we give estimates of the integrated event rate up to the 6 ms after merger.

Time [ms]	$\langle E_{\bar{\nu}_e}\rangle$ [MeV]	$\langle E_{\nu_e}\rangle$ [MeV]	$L_{\bar{\nu}_e}$ [10^{53} erg/s]	R_ν [#/ms]
02.5 (NL3)	18.5 (22.4)	15.2 (18.3)	0.71	18.1
03.0 (DD2)	18.3 (22.1)	14.6 (17.4)	1.1	28.2
03.2 (SFHo)	24.6 (29.7)	23.5 (28.3)	3.5	120.8
08.4 (NL3)	13.4 (15.6)	9.8 (11.3)	1.1	20.7
07.9 (DD2)	13.2 (16.1)	10.2 (12.4)	1.6	29.6

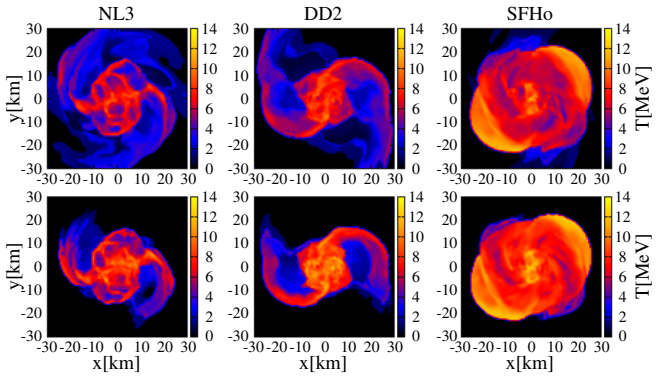

FIG. 16 (color online). Color map of the temperature at the scattering neutrinospheres at ~2.5 − 3 ms after merger for the NL3 EOS (left), DD2 EOS (center) and SFHo EOS (right). The top panels show the electron neutrinosphere, and the bottom panels show the electron antineutrinosphere.

(1) We assume that the luminosities shown in Fig. 15 are radiated isotropically from the merger. Observers situated along the merger axis would observe a larger than average neutrino luminosity, while observers situated on, or near, the equator would observe smaller average luminosities [98]. Therefore, the following predictions are the average expected rate over many sky orientations. (2) We assume the spectrum of neutrinos follows a zero chemical potential, Fermi-Dirac spectrum with a neutrino temperature that gives the average energy computed above ($\langle E_{\nu_i}\rangle \sim 3.15T_{\nu_i}$). (3) We assume that if an interaction occurs in the volume of the detector, it will be registered as an event. This may not be true for the lowest energy neutrinos, but such events should be few in number due to the low cross section. (4) Finally, as mentioned above, we neglect neutrino oscillations which may alter the electron antineutrino signal at Earth. Given these assumptions, the detection rate in a water-Cherenkov detector is then roughly given as

$$R_\nu \sim N_T \times n_\nu \times \frac{\int \mathcal{F}^2_{T_\nu}\sigma_{\text{IBD}}dE}{\int \mathcal{F}^2_{T_\nu}dE}, \tag{24}$$

where N_T is the number of target protons, which for the 32 kT Super-Kamiokande is equal to $2/18 \times 32 \times 10^9$ g/$m_{\text{amu}} \sim 2.1 \times 10^{33}$, $n_\nu = L/\langle E_\nu\rangle/(4\pi D^2)$ is the total number flux of neutrinos a distance D from the source, and $\int \mathcal{F}^2_{T_\nu}\sigma_{\text{IBD}}dE/\int \mathcal{F}^2_{T_\nu}dE$ is the spectrum weighted average cross section with $\mathcal{F}^2_T = E^2/[\exp(E/T)+1]$ equal to the zero-chemical potential Fermi-Dirac neutrino number distribution and where σ_{IBD} is the inverse-beta decay cross section, which can be approximated as $\sigma_{\text{IBD}} \sim \sigma_0/(4m_e^2)(1+3g_A^2)E^2_{\bar{\nu}_e}$ with $\sigma_0 = 1.761 \times 10^{-44}$ cm^2, $m_e = 0.511$ MeV, $g_A = -1.254$. All together, the detection rate is

$$R_\nu \sim \frac{21.1}{\text{ms}}\left[\frac{32\ \text{kT}}{M_{\text{water}}}\right]\left[\frac{L_\nu}{10^{53}\ \text{erg/s}}\right]\left[\frac{\langle E_\nu\rangle}{15\ \text{MeV}}\right]\left[\frac{10\ \text{kpc}}{D}\right]^2. \tag{25}$$

We have used Eq. (25)) to determine detection rates for the times and EOS listed in Table III. We take the electron antineutrino luminosities from Fig. 15 for the corresponding time and EOS (which we include in Table III for completeness). The resulting instantaneous detection rates for a merger located at 10 kpc from Earth in a detector like Super-Kamiokande are listed in the last column of Table III. To estimate the total number of neutrinos that can be detected, we take a fiducial length of time of 6 ms and integrate over Eq. (25) using the electron antineutrino luminosities shown in Fig. 15 and assuming a constant $\langle E_{\bar{\nu}_e} \rangle$ equal to the value near 3 ms in Table III. For the NL3, DD2, and SFHo EOS, we calculate ≈135, ≈176, ≈405 events, respectively, in the first 6 ms after merger in a Super-Kamiokande like detector and a merger event at ≈10 kpc. The merger with the SFHo EOS predicts much higher rates because both the luminosity and the average energy of the neutrinos is larger due to the higher matter temperatures achieved in the merger. If the resulting MNS collapses to a black hole (as in the SFHo case studied here), this could lead to a sharp reduction in the neutrino luminosity (e.g. Ref. [34]), otherwise, we would expect a slower decline in the neutrino luminosity as the MNS and disk cool. Ultimately many more events could be detected in the MNS/disk cooling phase, and both the total number and signal duration could strongly depend on the EOS [99].

One can ask how far would we be able to detect a BNS merger in neutrinos. As the distance of the merger increases, the rate of detection decreases quadratically, as seen in Eq. (25). For mergers similar to the ones studied here, but located in the Andromeda galaxy ∼800 kpc from Earth rather than 10 kpc, the detection rates are ∼6400 times smaller. Consequently, we would not expect any neutrinos in a detector like Super-Kamiokande. Detections with Super-Kamiokande would be limited to the Milky Way and surrounding satellite galaxies. However, with Hyper-Kamiokande, a future water-Cherenkov detector with a proposed volume ∼20 times that of Super-Kamiokande, the expected number of neutrinos in the first ∼10 ms would be $\mathcal{O}(1)$ and maybe a few over the entire lifetime of the disk, thus detectable especially in light of further timing input provided by gravitational waves.

D. Magnetic effects

We have also investigated the possible impact of magnetization within a time scale of ≈15 ms from the onset of the merger. To this end, we consider for simplicity the intermediate case (DD2) and endow the stars with a magnetic dipole of maximum strength 10^{13} G. The dynamics of the merger and early postmerger present several instabilities and processes capable of significantly amplifying the magnetization [21,22,100,101]. Indeed, recent local simulations have shown that some of these instabilities can drive the magnetic energy density up to a level approaching equipartition with the kinetic energy of the turbulent fluid on a time scale given by the turnover time of the resulting eddies [23,102]. However, these processes occur on very fine scales that require numerical resolution (and computational resources) generally beyond the reach of codes such as ours. Furthermore, with grid-based codes fully capturing these dynamics require resolutions of the order of $\lesssim$0.1 m.

Instead of such exorbitant resolutions, we introduce an "effective driver" mechanism (similar to those recently used in other papers [103,104]) to account for this amplification by including a term in the evolution equation for the magnetic field of the form

$$\partial_t(\sqrt{\gamma}B^i) = \cdots + \alpha\sqrt{\gamma}\xi B^i. \tag{26}$$

Here we have defined the amplification factor as

$$\xi \equiv \xi_0 \Theta(\rho[\omega^z - \omega^z_{\rm thresh}]) g(t) B_k v^k, \tag{27}$$

with $\Theta(x)$ the Heaviside function so that the amplification factor vanishes when the z-component of the fluid vorticity, ω^z, is below some threshold $\omega^z_{\rm thresh}$. This threshold is chosen to only activate this term for the eddies with wavelengths shorter than a third of the MNS radius. (This avoids, in particular, adding an additional increase to the magnetic field due to the star's differential rotation.) The factor $B_k v^k$ restricts the amplification only to the components along the velocity lines that stretch the magnetic field. The function $g(t)$ restricts when this subgrid model is active as described below. We note that the amplification introduced by this term is not explicitly divergence free. However, we monitor the divergence of the magnetic field, and find that, while it increases at merger, the rate of increase relative to the rate of increase of the field strength itself is comparable to that seen when the subgrid model is inactive.

This added term must be adjusted to match the expectations established by local simulations [23]. The term should result in the amplification of the magnetic field during merger until the associated magnetic energy density reaches strengths close to equipartition. In particular, small-scale dynamos act to amplify the magnetic field until the magnetic energy density reaches roughly ≈60% of the local turbulent kinetic energy density [23]. We therefore allow this subgrid model to act for a few milliseconds until the maximum magnetic field reaches 10^{16}–10^{17} G (see for instance Ref. [105] for a formal calculation of this turbulent kinetic energy). The bulk dynamics, combined with this subgrid model, give rise to a MNS with a strong and largely toroidal magnetic field structure. It is worth mentioning that we have tried an amplification factor without the factor $B_k v^k$ and obtained similar results. The ensuing topology is illustrated in Fig. 17.

We display the magnetic energy of the star in the top frame of Fig. 18. We call the evolution with no subgrid model our *low magnetization* case and compare it to the

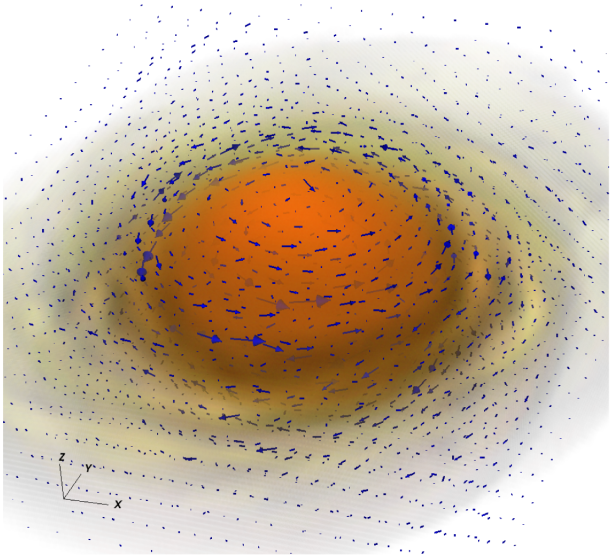

FIG. 17 (color online). Density (color map) and magnetic field vectors (blue arrows) for the high magnetization case at $t \approx 15$ ms after the merger, when the system has settled into a quasistationary configuration. The vectors show that the magnetic field is mostly toroidal.

case with the subgrid model active, our *high magnetization*. Also included in Fig. 18 are plots of the maximum density (middle panel) and the resulting GW signal (bottom panel). These figures reveal essentially no difference between the two magnetization cases within this time scale, despite

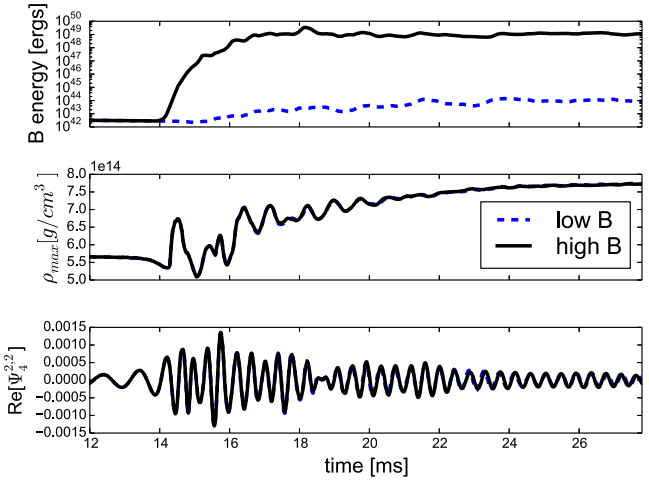

FIG. 18 (color online). Comparison of low and high magnetized cases for the DD2 binary. (top) The total magnetic energy for the domain. (middle) The maximum density for the two cases. (bottom) The primary mode of the GW signal. The merger takes place at $t \approx 14.3$ ms and during this merger the magnetic field grows significantly. Even for the high magnetization case in which $B_{\max} \approx 10^{17}$ G, the stellar dynamics remains largely unaffected as shown in the bottom two panels primarily because the magnetic field is mostly toroidal. Other quantities, such as the temperature and the neutrino radiation rate, also display small differences between low and high magnetizations.

the high magnetization case reaching almost 10^{17} G. Nevertheless, subtle differences arise with finer-scale phenomena.

We display the density, electron fraction, and magnetic field strength for both the low and high magnetization cases on a meridional plane in Fig. 19. A difference in electron fraction appears in the polar regions, but other differences are quite difficult to distinguish. So we compute the distributions of different quantities and display them in histograms. In particular, Fig. 20 displays the electron fraction for unbound material. While the low case has a flat distribution in Y_e, the high magnetization case peaks at roughly $Y_e \approx 0.15$. Note also that the high case ejects roughly twice the material of the low case, presumably due to the additional magnetic pressure. The angular distribution of the unbound matter is also shown in Fig. 20. The angular distribution suggests that the extra material unbound by the high magnetic field occurs primarily along equatorial directions.

The velocity distributions for both bound and unbound matter are shown in Fig. 21. The bound matter distributions

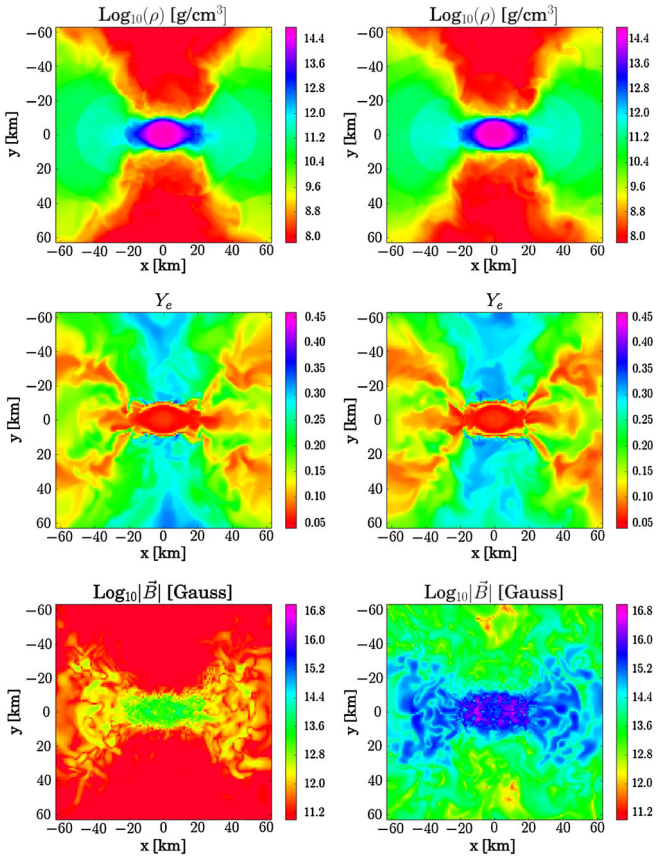

FIG. 19 (color online). Snapshots of density, electron fraction, and magnetic field strength in the meridional plane $x = 0$ at $t \approx 9$ ms after the merger, when the system has settled into a quasistationary configuration. The low magnetization case is displayed on the left and the high magnetization case is shown on the right.

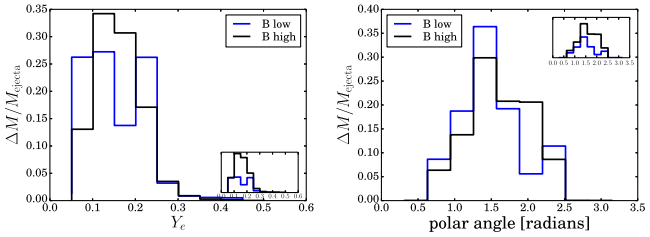

FIG. 20 (color online). Distributions of Y_e and angular direction for unbound stellar material for the low/high magnetized cases at $t \approx 9$ ms after the merger.

for the two cases are largely the same, but the unbound matter has a slightly higher average (but not peak) velocity for the high magnetization case.

Magnetic fields can also redistribute angular momentum and transport it from the inner to outer regions of the MNS [106]. Generally the processes that do this (e.g. magnetic breaking) take place over a time scale given by $\tau \approx R_{\rm MNS}/v_A$ with v_A the Alfven speed and R the radius of the star. For fields amplified to strengths of $\approx 10^{16}$ G, the time scale is roughly $\tau \approx 100$ ms and so a complete exploration of this possibility is rather costly. Nevertheless, we can extract indications of such a redistribution by comparing the behavior of the angular momentum for the low and high magnetization cases. Figure 22 shows the radially integrated value of the specific, z-component, angular momentum, l_z, within a given radius. Apparent in the figure is a small difference between the high and low cases. In particular, the highly magnetized case has less angular momentum at small radii than the weakly magnetized case, indicating that angular momentum has been transported outward. As a consequence, the contribution of rotational support against collapse weakens in the more magnetized case which could help induce a more prompt collapse to a black hole.

We note that the atmosphere used in these two magnetized cases is larger than the unmagnetized cases by 2 orders of magnitude. Because the differences that we see are largely where the outer material mixes with the atmosphere, it becomes difficult to isolate quantitative physical effects from atmosphere effects. Thus, the effects just discussed should be taken as qualitative indications while we work to

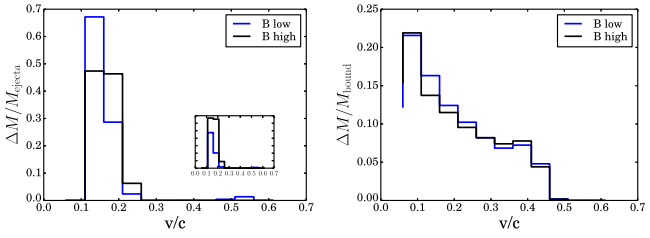

FIG. 21 (color online). Distributions of speeds for stellar material for the low/high magnetized cases at $t \approx 9$ ms after the merger.

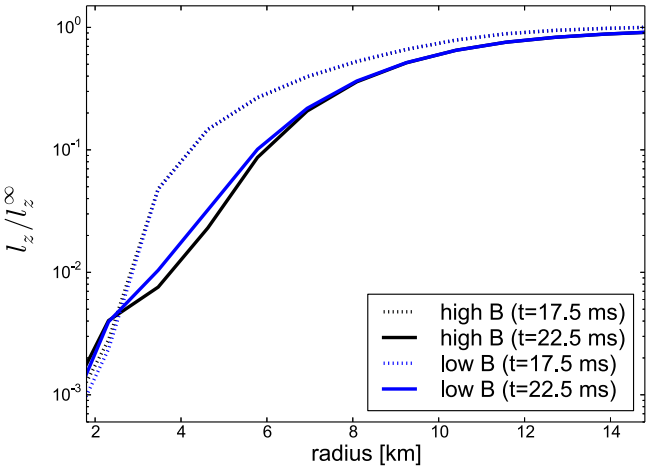

FIG. 22 (color online). Comparison of the radially integrated specific angular momentum component l_z for the low and high magnetized cases using the DD2 EOS at 3.2 and 8.2 ms after the merger takes place ($t = 17.5$ and 22.5 ms respectively). Angular momentum transport in the highly magnetized case is stronger and, as a result, its integrated value in the central region of the MNS is smaller than its lower magnetized counterpart case.

further improve the treatment of the atmosphere. (We note that we have performed several tests to ensure the results presented here can be trusted. In particular, for the low magnetization case we have run with an atmosphere level lower by 2 orders of magnitude and compared at what time differences arose. This allowed us to identify the time frame during which the relevant dynamics is not affected by the higher atmosphere.)

IV. CONCLUSIONS

In this paper we have explored the rich phenomenology of binary mergers of equal mass neutron stars using realistic equations of state, neutrino cooling, and electromagnetic effects. Our results indicate a tight connection between different possible observables and the neutron star EOS. In addition to the impact of the equation of state on gravitational waves that are emitted during and after the merger, both neutrino production and the properties of ejected material are strongly dependent on the EOS (which, in turn, would have a strong impact on electromagnetic signals from radioactive decay). We also developed a subgrid model designed to capture the amplification of the magnetic field generated by turbulent flow during the merger. We find indications of increased angular momentum transport with the amplified magnetic field, though a detailed analysis is left to a future paper.

The EOS imprints subtle differences on the expected GW signals prior (but close) to merger, and these differences become much more significant during merger and afterward. With softer equations of state, for example, the merger occurs at higher frequencies than for stiffer equations of state. The orbital frequency at merger exerts a

strong influence on the resulting MNS. In particular, an analysis of the dominant frequency components of the gravitational signal after merger reveals that they can be roughly approximated by this orbital frequency at merger together with the characteristic oscillations of the MNS. Our results suggest that the three waveforms presented here may be distinguishable by aLIGO for optimal configurations up to distances of ≈120 Mpc (without assuming other techniques like stacking of signals to further enhance this possibility). These results are consistent with those found in [33].

An analysis of the neutrino production indicates that EOS yielding more compact stars (softer EOS) produce the largest neutrino luminosity with the highest average neutrino energy. As discussed, this is intuitively expected as the collision takes place deeper in the gravitational potential with a more violent collision. We estimate that neutrinos produced by these mergers could be observed anywhere in the Milky Way or surrounding satellite galaxies with current neutrino detectors such as Super-Kamiokande. Using larger detector volumes like the proposed Hyper-Kamiokande detector, the mergers studied here predict that we would see $\mathcal{O}(1)$ neutrinos within the first ≈10–20 ms after merger.

An analysis of the ejecta indicates that only the softest EOS yields sufficient material, and of the right quality, to power a kilonova event peaking in the infrared. Indications such as this are of significant current interest in light of the recent observations reported in [14–16]. These observations found an infrared emission occurring roughly a week after sGRB 130603B and about thirteen days after GRB-060614, consistent with predictions of the decay of heavy r-process elements. That softer EOS merge through a more violent collision sets the proper stage for a large amount of quite neutron rich ejecta, a requirement for producing heavy elements through r-processes which, in turn, can produce an observable infrared emission through their radioactive decay.

Finally, it is then interesting to connect these observations with our numerical results to speculate about the neutron star EOS. As has been discussed in, for example, Ref. [37], nonvacuum compact binaries are the prime candidates for producing heavy elements through r-process nucleosynthesis. Such binaries are favored because of: (i) the mounting evidence connecting compact binary mergers with sGRBs (e.g. [17]) and (ii) the observational indications [36] that supernovae fail to produce such heavy elements. If indeed these binaries are the primary producers of the heavy elements and if sGRB 130603B and GRB 060614 are representative, then one can speculate that the neutron star EoS is a soft one. Simulations presented here and also in Ref. [34] indicate that intermediate and stiff EoS are unable to eject enough material with a sufficiently high neutron composition, and this result, at the least, is suggestive that neutron stars are described by a soft EOS.

However, this line of reasoning is speculative and further numerical work is needed. In particular, the properties of ejecta resulting from the merger of unequal mass neutron stars are yet to be analyzed, but simulations have shown that mergers of unequal binaries can generate accretion disks more massive than those produced by equal mass binaries [107,108]. It thus would appear possible that the amount of ejecta and its properties might depend sensitively on the mass ratio. Such studies are thus an important priority, although observational evidence points to small mass ratios in binary neutron star systems [109].

An alternative path could be provided by black hole-neutron star binaries. (Ejecta estimates in such mergers have been examined recently in [94,110].) However for sufficient ejecta with the required neutron richness, the black hole spin has to be quite high, the ratio of black hole mass to neutron star mass should be small, and the stellar EOS needs to be stiff. These ingredients enhance the possibility of tidal disruption. However observed black hole masses and stellar black hole spin estimates (see e.g. [111]), if they hold generally, indicate black hole masses $> 8M_{\odot}$ with any possible spin. Therefore, the likelihood of r-process nucleosynthesis occurring in black hole–neutron star binaries remains unclear.

It is certainly quite interesting that these two possible paths—binary neutron star or black-hole neutron star mergers—seem to prefer two very distinct possibilities for the EOS to yield kilonova events like the ones reported. Excitingly, based on current observational evidence, a single gravitational wave observation tied to a sGRB might be enough to single out the correct case.

ACKNOWLEDGMENTS

It is a pleasure to thank Jolien Creighton, Rodrigo Fernandez, Chad Hanna, Jonnas Lipuner, Albino Perego, and Eliot Quataert for interesting discussions as well as our collaborators Eric Hirschmann, Patrick Motl, and Marcelo Ponce. This work was supported by the NSF under Grants No. PHY-1308621 (LIU), No. PHY-0969811 and No. PHY-1308727 (BYU), NASA's ATP program through Grant No. NNX13AH01G, NSERC through a Discovery Grant (to L. L.) and CIFAR (to L. L.). C. P. acknowledges support from the Spanish Ministry of Education and Science through a Ramon y Cajal grant and from the Spanish Ministry of Economy and Competitiveness Grant No. FPA2013-41042-P. Additional support for this work was provided by NASA through Hubble Fellowship Grant No. 51344.001-A awarded by the Space Telescope Science Institute, which is operated by the Association of Universities for Research in Astronomy, Inc., for NASA, under Contract No. NAS 5-26555. Research at Perimeter Institute is supported through Industry Canada and by the Province of Ontario through the Ministry of Research & Innovation. Computations were performed at XSEDE and Scinet.

APPENDIX A: THE PRIMITIVE SOLVER

High-resolution shock-capturing schemes integrate the fluid equations in conservation form for the conservative variables, while the fluid equations are written in a mixture of conserved and primitive variables. It is well known that the calculation of primitive variables from conserved variables for relativistic fluids requires solving a transcendental set of equations. Our method for solving these equations with a finite-temperature EOS is a modification of the algorithm that we use for the ideal gas EOS; the most significant change being that the internal energy must be calculated separately from the pressure using the table.

The evolved conserved variables are defined as

$$D \equiv \rho W \tag{A1}$$

$$S_i \equiv (hW^2 + B^2)v_i - (B^j v_j)B_i \tag{A2}$$

$$\tau \equiv hW^2 + B^2 - P - \frac{1}{2}\left((B^i v_i)^2 + \frac{B^2}{W^2}\right) \tag{A3}$$

$$DY_e \equiv \rho W Y_e. \tag{A4}$$

The dominant energy condition places constraints on the allowed values of the conserved variables,

$$D \geq 0, \qquad S^2 \leq (D+\tau)^2, \qquad DY_e \geq 0, \tag{A5}$$

and depending on the EOS the second condition can be sharpened to $S^2 \leq (2D+\tau)\tau$ [112]. These constraints may be violated during the evolution due to numerical error, and they are enforced before solving for the primitive variables. A minimum allowable value of the conserved density $D_{\rm vac}$ is chosen, and if D falls below this value we set $v^i = 0$ and $D \to D_{\rm vac}$. We choose $D_{\rm vac}$ as low as possible for the unmagnetized neutron star binary, which is about 9 orders of magnitude smaller than the initial central density of the stars. For the magnetized case our solver fails for such tenuous atmospheres, and it is increased by 2 orders of magnitude. If the second inequality is violated, then the magnitude of S_i is rescaled to satisfy the inequality. Finally, DY_e is required to satisfy the constraint on D, and the computed value of Y_e must be in the equation of state table.

The primitives to be found are the density, ρ, pressure P, electron fraction Y_e, internal energy density ϵ (i.e., or the temperature T, once the EOS is known) and velocity three-vector v^i. The magnetic field is at the same time conserved and primitive field. We write the transcendental equations in terms of the new rescaled variable

$$x \equiv \frac{hW^2}{\rho W}, \tag{A6}$$

where h is the *total* enthalpy $h \equiv \rho(1+\epsilon) + P$, and calculate Y_e from the evolution variables DY_e/D. Following [113], we rescale the conserved fields in order to get order-unity quantities, namely,

$$q \equiv \tau/D, \qquad r \equiv S^2/D^2,$$
$$s \equiv B^2/D, \qquad t \equiv B_i S^i/D^{3/2}. \tag{A7}$$

Then, using data from the previous time step to calculate an initial guess for x, we iteratively solve these equations for x within the bounds

$$1 + q - s > x > 2 + 2q - s, \tag{A8}$$

so that the final procedure can be written as

(1) From the equation for $S^i S_i$, calculate an approximate Lorentz factor $\hat{W}$:

$$\hat{W}^{-2} = 1 - \frac{x^2 r + (2x+s)t^2}{x^2(x+s)^2}.$$

(2) From the definition of D, calculate

$$\hat{\rho} = \frac{D}{\hat{W}}.$$

(3) From the definition of τ and the total enthalpy, calculate

$$\hat{\epsilon} = \hat{W} - 1 + \frac{x}{\hat{W}}(1 - \hat{W}^2) + \hat{W}\left[q - s + \frac{t^2}{2x^2} + \frac{s}{2\hat{W}^2}\right].$$

(4) Use the EOS table to calculate the pressure $P(\hat{\rho}, \hat{\epsilon}, Y_e)$.

(5) Update the guess for x by solving the equation $f(x) = 0$ using the Brent method, being $f(x)$ just the definition of the unknown x,

$$f(x) = x - \left(1 + \hat{\epsilon} + \frac{P(\hat{\rho}, \hat{\epsilon}, Y_e)}{\hat{\rho}}\right)\hat{W}.$$

The root of $f(x) = 0$ from step 5 becomes the new guess for x, and this process is repeated iteratively until the solution for x converges to a specified tolerance, which is ensured if there is a physical solution within the bounds. One advantage of this algorithm is that $f(x)$ is a function of a single variable, and, in contrast to a multiple variable search for a root, robust methods can be used to find any root that can be bracketed.

Because of numerical error, a solution to these equations may either fall outside the physical range for the primitive variables, or a real solution for x may not exist. The solutions for ρ, T, and Y_e are, at a minimum, restricted to

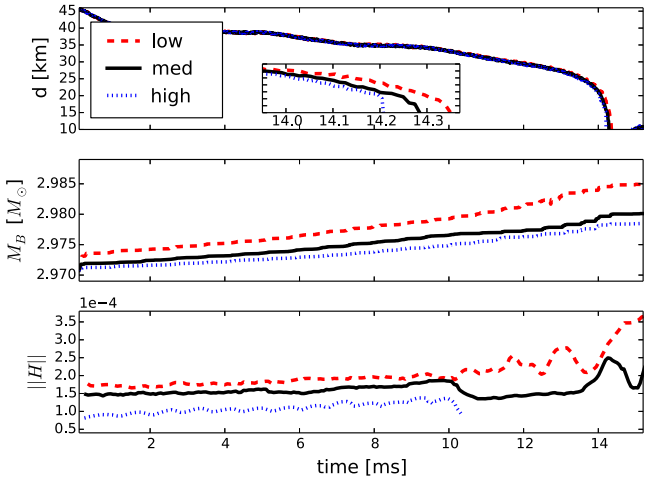

FIG. 23 (color online). The stellar separation, d (top), the total baryonic mass, M_B (middle), and the l2-norm of the Hamiltonian constraint residual, $\|H\|$ (bottom), as functions of time for the DD2 EOS with three different resolutions $\Delta x = \{275, 230, 192\}$ m. (The data for the Hamiltonian constraint residual for the highest resolution beyond $t = 10$ ms was accidentally lost.)

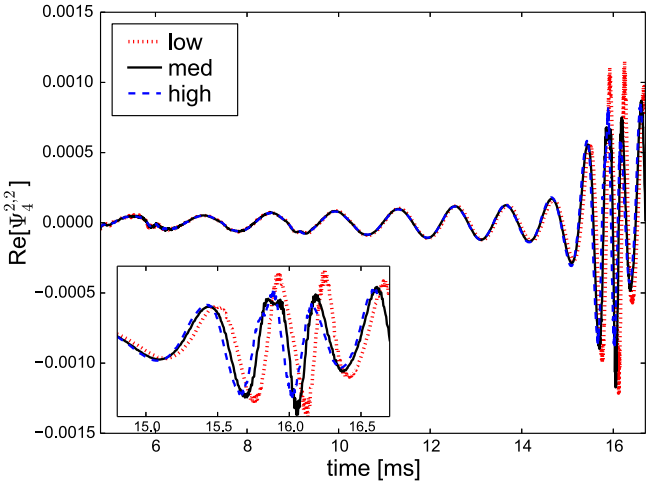

FIG. 24 (color online). The convergence of the principal $l = m = 2$ mode of Ψ_4 for the same cases as shown in Fig. 23.

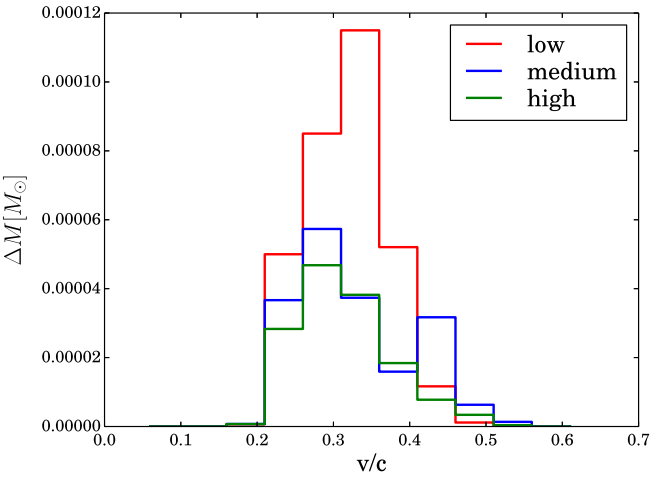

FIG. 25 (color online). Histogram of the velocities, computed a few milliseconds after merger for the same cases as shown in Fig. 23. Notice that the medium and high resolution results have largely converged.

values in the table, and they are reset to new values (the minimum allowed value plus ten percent) if necessary. If a real solution for the primitive variables does not exist, the primitive variables are interpolated from neighboring points, and the conserved variables are reset to be consistent. If a valid interpolation stencil cannot be constructed because the solver also failed at the neighboring points, then the update fails, and the run is terminated. This failure occurs very rarely and may be remedied by slightly increasing the density floor $D_{\rm vac}$.

APPENDIX B: CONVERGENCE TESTS

The inspiral and merger of two neutron stars is a significant test due to the inherent asymmetry of the problem that tends to "excite" many, if not all, terms in the equations. Resolving both the motion of two compact objects as well as the large gradients at their surfaces requires significant resources. The merger itself is a very dynamic process with a large range of densities. Therefore, a study of the convergence of the numerical solution is necessary to assess the validity of our results.

We have evolved a binary using the DD EOS with three different resolutions (i.e., low, medium, and high) corresponding to $\Delta x = \{275, 230, 192\}$ m. The stellar separation, the total baryonic mass (which should be strictly conserved during the evolution) and the Hamiltonian constraint (which should converge to zero) are displayed in Fig. 23. Interestingly, the merger happens at earlier times for higher resolutions, a trend opposite of that reported elsewhere. This might indicate that the source of our numerical errors has a different sign. In any case, the results converge at order $\approx$1.9.

The convergence of the principal $l = m = 2$ mode of Ψ_4 is shown in Fig. 24. Finally, the distribution of the velocity of the fluid, computed just a few milliseconds after merger, is displayed for the different resolutions in Fig. 25.

[1] J. Abadie, B. P. Abbott, R. Abbott, M. Abernathy, T. Accadia, F. Acernese, C. Adams, R. Adhikari, P. Ajith, B. Allen *et al.*, Topical review: Predictions for the rates of compact binary coalescences observable by ground-based gravitational-wave detectors, Classical Quantum Gravity **27**, 173001 (2010).

[2] C. Palenzuela, L. Lehner, M. Ponce, S. L. Liebling, M. Anderson, D. Neilsen, and P. Motl, Gravitational and Electromagnetic Outputs from Binary Neutron Star Mergers, Phys. Rev. Lett. **111**, 061105 (2013).

[3] C. Palenzuela, L. Lehner, S. L. Liebling, M. Ponce, M. Anderson, D. Neilsen, and P. Motl, Linking electromagnetic and gravitational radiation in coalescing binary neutron stars, Phys. Rev. D **88**, 043011 (2013).

[4] M. Ponce, C. Palenzuela, L. Lehner, and S. L. Liebling, Interaction of misaligned magnetospheres in the coalescence of binary neutron stars, Phys. Rev. D **90**, 044007 (2014).

[5] D. Tsang, J. S. Read, T. Hinderer, A. L. Piro, and R. Bondarescu, Resonant Shattering of Neutron Star Crusts, Phys. Rev. Lett. **108**, 011102 (2012).

[6] M. Shibata and K. Uryu, Merger of black hole–neutron star binaries in full general relativity, Classical Quantum Gravity **24**, S125 (2007).

[7] Z. B. Etienne, Y. T. Liu, S. L. Shapiro, and T. W. Baumgarte, General relativistic simulations of black-hole-neutron-star mergers: Effects of black-hole spin, Phys. Rev. D **79**, 044024 (2009).

[8] S. Chawla, M. Anderson, M. Besselman, L. Lehner, S. L. Liebling, P. M. Motl, and D. Neilsen, Mergers of Magnetized Neutron Stars with Spinning Black Holes: Disruption, Accretion and Fallback, Phys. Rev. Lett. **105**, 111101 (2010).

[9] F. Foucart, L. Buchman, M. D. Duez, M. Grudich, L. E. Kidder, I. MacDonald, A. Mroue, H. P. Pfeiffer, M. A. Scheel, and B. Szilagyi, First direct comparison of nondisrupting neutron star-black hole and binary black hole merger simulations, Phys. Rev. D **88**, 064017 (2013).

[10] L.-X. Li and B. Paczynski, Transient events from neutron star mergers, Astrophys. J. **507**, L59 (1998).

[11] S. Kulkarni, Modeling supernova-like explosions associated with gamma-ray bursts with short durations, arXiv: astro-ph/0510256.

[12] B. Metzger, A. Piro, and E. Quataert, Time-dependent models of accretion disks formed from compact object mergers, Mon. Not. R. Astron. Soc. **390**, 781 (2008).

[13] D. Kasen, R. Fernandez, and B. Metzger, Kilonova light curves from the disk wind outflows of compact object mergers, Mon. Not. R. Astron. Soc. **450**, 1777 (2015).

[14] N. R. Tanvir, A. J. Levan, A. S. Fruchter, J. Hjorth, R. A. Hounsell, K. Wiersema, and R. L. Tunnicliffe, A "kilonova", associated with the short-duration γ-ray burst GRB 130603B, Nature (London) **500**, 547 (2013).

[15] E. Berger, W. Fong, and R. Chornock, An r-process kilonova associated with the short-hard GRB 130603B, Astrophys. J. **774**, L23 (2013).

[16] B. Yang, Z.-P. Jin, X. Li, S. Covino, X.-Z. Zheng, K. Hotokezaka, Yi-Zhong Fan, T. Piran, and Da-Ming Wei, A possible Macronova in the late afterglow of the "long-short" burst GRB 060614, Nat. Commun. **6**, 7323 (2015).

[17] E. Berger, Short-duration gamma-ray bursts, Annu. Rev. Astron. Astrophys. **52**, 43 (2014).

[18] Y. Sekiguchi, K. Kiuchi, K. Kyutoku, and M. Shibata, Current status of numerical-relativity simulations in Kyoto, Prog. Theor. Exp. Phys. **2012**, 01A304 (2012).

[19] C. L. Fryer, K. Belczynski, E. Ramirez-Ruiz, S. Rosswog, G. Shen *et al.*, The fate of the compact remnant in neutron star mergers, arXiv:1504.07605.

[20] W. Kastaun, F. Galeazzi, D. Alic, L. Rezzolla, and J. A. Font, Black hole from merging binary neutron stars: How fast can it spin?, Phys. Rev. D **88**, 021501 (2013).

[21] D. J. Price and S. Rosswog, Producing ultrastrong magnetic fields in neutron star mergers, Science **312**, 719 (2006).

[22] M. Anderson, E. W. Hirschmann, L. Lehner, S. L. Liebling, P. M. Motl, D. Neilsen, C. Palenzuela, and Joel E. Tohline, Magnetized Neutron Star Mergers and Gravitational Wave Signals, Phys. Rev. Lett. **100**, 191101 (2008).

[23] J. Zrake and A. I. MacFadyen, Magnetic energy production by turbulence in binary neutron star mergers, Astrophys. J. **769**, L29 (2013).

[24] J. S. Read, C. Markakis, M. Shibata, K. Uryū, J. D. E. Creighton, and J. L. Friedman, Measuring the neutron star equation of state with gravitational wave observations, Phys. Rev. D **79**, 124033 (2009).

[25] L. Baiotti, T. Damour, B. Giacomazzo, A. Nagar, and L. Rezzolla, Accurate numerical simulations of inspiralling binary neutron stars and their comparison with effective-one-body analytical models, Phys. Rev. D **84**, 024017 (2011).

[26] T. Damour, A. Nagar, and L. Villain, Measurability of the tidal polarizability of neutron stars in late-inspiral gravitational-wave signals, Phys. Rev. D **85**, 123007 (2012).

[27] L. Lehner, C. Palenzuela, S. L. Liebling, C. Thompson, and C. Hanna, Intense electromagnetic outbursts from collapsing hypermassive neutron stars, Phys. Rev. D **86**, 104035 (2012).

[28] K. Kyutoku, K. Ioka, and M. Shibata, Ultrarelativistic counterparts to binary neutron star mergers in every direction, x-ray-to-radio bands and second-to-day time scales, Mon. Not. R. Astron. Soc. **437**, L6 (2014).

[29] B. D. Metzger and E. Berger, What is the most promising electromagnetic counterpart of a neutron star binary merger?, Astrophys. J. **746**, 48 (2012).

[30] N. Andersson, J. Baker, K. Belczynski, S. Bernuzzi, E. Berti *et al.*, The transient gravitational-wave sky, Classical Quantum Gravity **30**, 193002 (2013).

[31] L. Rezzolla and P. Kumar, A novel paradigm for short gamma-ray bursts with extended x-ray emission, Astrophys. J. **802**, 95 (2015).

[32] D. Neilsen, S. L. Liebling, M. Anderson, L. Lehner, E. O'Connor, and C. Palenzuela, Magnetized neutron stars with realistic equations of state and neutrino cooling, Phys. Rev. D **89**, 104029 (2014).

[33] J. S. Read, L. Baiotti, J. D. E. Creighton, J. L. Friedman, B. Giacomazzo, K. Kyutoku, C. Markakis, L. Rezzolla, M. Shibata, and K. Taniguchi, Matter effects on binary neutron star waveforms, Phys. Rev. D **88**, 044042 (2013).

[34] Y. Sekiguchi, K. Kiuchi, K. Kyutoku, and M. Shibata, Dynamical mass ejection from binary neutron star mergers: Radiation-hydrodynamics study in general relativity, Phys. Rev. D **91**, 064059 (2015).
[35] K. Hotokezaka, K. Kiuchi, K. Kyutoku, H. Okawa, Y.-i. Sekiguchi, M. Shibata, and K. Taniguchi, Mass ejection from the merger of binary neutron stars, Phys. Rev. D **87**, 024001 (2013).
[36] A. Wallner, T. Faestermann, J. Feige, C. Feldstein, K. Knie, G. Korschinek, W. Kutschera, A. Ofan, M. Paul, F. Quinto, G. Rugel, and P. Steier, Abundance of live ^{244}Pu in deep-sea reservoirs on Earth points to rarity of actinide nucleo-synthesis, Nat. Commun. **6**, 5956 (2015).
[37] T. Piran, O. Korobkin, and S. Rosswog, Implications of GRB 130603B and its macronova for r-process nucleo-synthesis, arXiv:1401.2166.
[38] M. Anderson, E. Hirschmann, S. L. Liebling, and D. Neilsen, Relativistic MHD with adaptive mesh refinement, Classical Quantum Gravity **23**, 6503 (2006).
[39] S. L. Liebling, L. Lehner, D. Neilsen, and C. Palenzuela, Evolutions of magnetized and rotating neutron stars, Phys. Rev. D **81**, 124023 (2010).
[40] T. Nakamura, K. Oohara, and Y. Kojima, General relativistic collapse to black holes and gravitational waves from black holes, Prog. Theor. Phys. Suppl. **90**, 1 (1987).
[41] M. Shibata and T. Nakamura, Evolution of three-dimensional gravitational waves: Harmonic slicing case, Phys. Rev. D **52**, 5428 (1995).
[42] T. W. Baumgarte and S. L. Shapiro, Numerical integration of Einstein's field equations, Phys. Rev. D **59**, 024007 (1998).
[43] M. Campanelli, C. O. Lousto, P. Marronetti, and Y. Zlochower, Accurate Evolutions of Orbiting Black-Hole Binaries without Excision, Phys. Rev. Lett. **96**, 111101 (2006).
[44] C. Palenzuela, L. Lehner, O. Reula, and L. Rezzolla, Beyond ideal MHD: Towards a more realistic modeling of relativistic astrophysical plasmas, Mon. Not. R. Astron. Soc. **394**, 1727 (2009).
[45] C. Palenzuela, Modeling magnetized neutron stars using resistive magnetohydrodynamics, Mon. Not. R. Astron. Soc. **431**, 1853 (2013).
[46] G. Calabrese, L. Lehner, D. Neilsen, J. Pullin, O. Reula, O. Sarbach, and M. Tiglio, Novel finite-differencing techniques for numerical relativity: Application to black hole excision, Classical Quantum Gravity **20**, L245 (2003).
[47] G. Calabrese, L. Lehner, O. Reula, O. Sarbach, and M. Tiglio, Summation by parts and dissipation for domains with excised regions, Classical Quantum Gravity **21**, 5735 (2004).
[48] C.-W. Shu and S. Osher, Efficient implementation of essentially nonoscillatory shock-capturing schemes, J. Comput. Phys. **77**, 439 (1988).
[49] M. Anderson, E. W. Hirschmann, L. Lehner, S. L. Liebling, P. M. Motl, D. Neilsen, C. Palenzuela, and J. E. Tohline, Simulating binary neutron stars: Dynamics and gravitational waves, Phys. Rev. D **77**, 024006 (2008).
[50] HAD home page: http://had.liu.edu.
[51] S. L. Liebling, The singularity threshold of the nonlinear sigma model using 3d adaptive mesh refinement, Phys. Rev. D **66**, 041703 (2002).
[52] L. Lehner, S. L. Liebling, and O. Reula, AMR, stability and higher accuracy, Classical Quantum Gravity **23**, S421 (2006).
[53] STELLARCOLLAPSE home page: http://www.stellarcollapse.org.
[54] E. O'Connor and C. D. Ott, A new open-source code for spherically symmetric stellar collapse to neutron stars and black holes, Classical Quantum Gravity **27**, 114103 (2010).
[55] M. Brett Deaton, M. D. Duez, F. Foucart, E. O'Connor, C. D. Ott, L. E. Kidder, C. D. Muhlberger, M. A. Scheel, and B. Szilagyi, Black hole-neutron star mergers with a hot nuclear equation of state: Outflow and neutrino-cooled disk for a low-mass, high-spin case, Astrophys. J. **776**, 47 (2013).
[56] E. Newman and R. Penrose, An approach to gravitational radiation by a method of spin coefficients, J. Math. Phys. (N.Y.) **3**, 566 (1962).
[57] E. T. Newman and K. P. Tod, *Asymptotically flat space-times* (Plenum, New York, 1982), Vol. 2, pp. 1–36.
[58] L. Lehner and O. M. Moreschi, Dealing with delicate issues in waveform calculations, Phys. Rev. D **76**, 124040 (2007).
[59] M. Boyle, D. A. Brown, L. E. Kidder, A. H. Mroué, H. P. Pfeiffer, M. A. Scheel, G. B. Cook, and S. A. Teukolsky, High-accuracy comparison of numerical relativity simulations with post-Newtonian expansions, Phys. Rev. D **76**, 124038 (2007).
[60] J. Vines, E. E. Flanagan, and T. Hinderer, Post-1-Newtonian tidal effects in the gravitational waveform from binary inspirals, Phys. Rev. D **83**, 084051 (2011).
[61] K. Hotokezaka, K. Kyutoku, and M. Shibata, Exploring tidal effects of coalescing binary neutron stars in numerical relativity, Phys. Rev. D **87**, 044001 (2013).
[62] Super-Kamiokande, http://www-sk.icrr.u-tokyo.ac.jp/sk/index-e.html.
[63] IceCube, https://icecube.wisc.edu/.
[64] Hyper-Kamiokande, http://www.hyperk.org.
[65] L. Z. Kelley, I. Mandel, and E. Ramirez-Ruiz, Electromagnetic transients as triggers in searches for gravitational waves from compact binary mergers, Phys. Rev. D **87**, 123004 (2013).
[66] B. Metzger and E. Berger, What is the most promising electromagnetic counterpart of a neutron star binary merger?, Astrophys. J. **746**, 48 (2012).
[67] L. Lehner and F. Pretorius, Numerical relativity and astrophysics, Annu. Rev. Astron. Astrophys. **52**, 661 (2014).
[68] J. M. Lattimer, The nuclear equation of state and neutron star masses, Annu. Rev. Nucl. Part. Sci. **62**, 485 (2012).
[69] A. W. Steiner, M. Hempel, and T. Fischer, Core-collapse supernova equations of state based on neutron star observations, Astrophys. J. **774**, 17 (2013).
[70] M. Hempel, T. Fischer, J. Schaffner-Bielich, and M. Liebendörfer, New equations of state in simulations of core-collapse supernovae, Astrophys. J. **748**, 70 (2012).

[71] P. Demorest, T. Pennucci, S. Ransom, M. Roberts, and J. Hessels, Shapiro delay measurement of a two solar mass neutron star, Nature (London) **467**, 1081 (2010).

[72] J. Antoniadis, P. C. Freire, N. Wex, T. M. Tauris, R. S. Lynch *et al.*, A massive pulsar in a compact relativistic binary, Science **340**, 1233232 (2013).

[73] LORENEhome page: http://www.lorene.obspm.fr/.

[74] K. Ioka and K. Taniguchi, Gravitational waves from inspiralling compact binaries with magnetic dipole moments, Astrophys. J. **537**, 327 (2000).

[75] E. Poisson and C. M. Will, *Gravity: Newtonian, Post-Newtonian, Relativistic* (Cambridge University Press, Cambridge, 2014), ISBN 9781107032866.

[76] A. Buonanno and T. Damour, Effective one-body approach to general relativistic two-body dynamics, Phys. Rev. D **59**, 084006 (1999).

[77] A. Buonanno, L. E. Kidder, and L. Lehner, Estimating the final spin of a binary black hole coalescence, Phys. Rev. D **77**, 026004 (2008).

[78] F. Foucart, Black hole-neutron star mergers: Disk mass predictions, Phys. Rev. D **86**, 124007 (2012).

[79] S. Bernuzzi, A. Nagar, T. Dietrich, and T. Damour, Modeling the Dynamics of Tidally Interacting Binary Neutron Stars up to the Merger, Phys. Rev. Lett. **114**, 161103 (2015).

[80] G. B. Cook, S. L. Shapiro, and S. A. Teukolsky, Rapidly rotating neutron stars in general relativity: Realistic equations of state, Astrophys. J. **424**, 823 (1994).

[81] A. Bauswein and N. Stergioulas, A unified picture of the post-merger dynamics and gravitational wave emission in neutron-star mergers, Phys. Rev. D **91**, 124056 (2015).

[82] An empirical fit to the peak frequency can also be obtained as in [81].

[83] B. Abbott *et al.* (LIGO Scientific Collaboration), Stacked search for gravitational waves from the 2006 SGR 1900 + 14 storm, Astrophys. J. **701**, L68 (2009).

[84] W. Kastaun and F. Galeazzi, Properties of hypermassive neutron stars formed in mergers of spinning binaries, Phys. Rev. D **91**, 064027 (2015).

[85] K. Takami, L. Rezzolla, and L. Baiotti, Spectral properties of the post-merger gravitational-wave signal from binary neutron stars, Phys. Rev. D **91**, 064001 (2015).

[86] Ligo document t0900288-v3, https://dcc.ligo.org/cgi-bin/DocDB/ShowDocument?docid=2974.

[87] B. J. Owen, Search templates for gravitational waves from inspiraling binaries: Choice of template spacing, Phys. Rev. D **53**, 6749 (1996).

[88] T. Baumgarte, P. R. Brady, J. D. E. Creighton, L. Lehner, F. Pretorius, and R. DeVoe, Learning about compact binary merger: The interplay between numerical relativity and gravitational-wave astronomy, Phys. Rev. D **77**, 084009 (2008).

[89] E. Nakar, Short-hard gamma-ray bursts, Phys. Rep. **442**, 166 (2007).

[90] A. Murguia-Berthier, G. Montes, E. Ramirez-Ruiz, F. De Colle, and W. H. Lee, Necessary conditions for short gamma-ray burst production in binary neutron star mergers, Astrophys. J. **788**, L8 (2014).

[91] R. Fernndez, E. Quataert, J. Schwab, D. Kasen, and S. Rosswog, The interplay of disk wind and dynamical ejecta in the aftermath of neutron star–black hole mergers, Mon. Not. R. Astron. Soc. **449**, 390 (2015).

[92] J. Lippuner (private communication).

[93] Y. Sekiguchi, K. Kiuchi, K. Kyutoku, and M. Shibata, Gravitational Waves and Neutrino Emission from the Merger of Binary Neutron Stars, Phys. Rev. Lett. **107**, 051102 (2011).

[94] F. Foucart, E. O'Connor, L. Roberts, M. D. Duez, R. Haas, L. E. Kidder, C. D. Ott, H. P. Pfeiffer, M. A. Scheel, and B. Szilagyi, Post-merger evolution of a neutron star-black hole binary with neutrino transport, Phys. Rev. D **91**, 124021 (2015).

[95] M. Ruffert, H.-T. Janka, K. Takahashi, and G. Schaefer, Coalescing neutron stars—A step towards physical models. II. Neutrino emission, neutron tori, and gamma-ray bursts, Astron. Astrophys. **319**, 122 (1997).

[96] A. Malkus, A. Friedland, and G. C. McLaughlin, Matter-neutrino resonance above merging compact objects, arXiv:1403.5797.

[97] O. L. Caballero, G. C. McLaughlin, and R. Surman, Detecting neutrinos from black hole-neutron star mergers, Phys. Rev. D **80**, 123004 (2009).

[98] A. Perego, S. Rosswog, R. M. Cabezón, O. Korobkin, R. Käppeli, A. Arcones, and M. Liebendörfer, Neutrino-driven winds from neutron star merger remnants, Mon. Not. R. Astron. Soc. **443**, 3134 (2014).

[99] O. Just, A. Bauswein, R. A. Pulpillo, S. Goriely, and H.-T. Janka, Comprehensive nucleosynthesis analysis for ejecta of compact binary mergers, Mon. Not. R. Astron. Soc. **448**, 541 (2015).

[100] M. Obergaulinger, M. A. Aloy, and E. Muller, Local simulations of the magnetized Kelvin-Helmholtz instability in neutron-star mergers, arXiv:1003.6031.

[101] K. Kiuchi, K. Kyutoku, Y. Sekiguchi, M. Shibata, and T. Wada, High resolution numerical-relativity simulations for the merger of binary magnetized neutron stars, Phys. Rev. D **90**, 041502 (2014).

[102] M. Obergaulinger, M. A. Aloy, and E. Müller, Local simulations of the magnetized Kelvin-Helmholtz instability in neutron-star mergers, Astron. Astrophys. **515**, A30 (2010).

[103] B. Giacomazzo, J. Zrake, P. Duffell, A. I. MacFadyen, and R. Perna, Producing magnetar magnetic fields in the merger of binary neutron stars, arXiv:1410.0013.

[104] A. Sądowski, R. Narayan, A. Tchekhovskoy, D. Abarca, Y. Zhu, and J. C. McKinney, Global simulations of axisymmetric radiative black hole accretion disks in general relativity with a mean-field magnetic dynamo, Mon. Not. R. Astron. Soc. **447**, 49 (2015).

[105] P. C. Duffell and A. I. MacFadyen, Rayleigh-Taylor instability in a relativistic fireball on a moving computational grid, Astrophys. J. **775**, 87 (2013).

[106] L. Mestel, *Stellar Magnetism* (Oxford University Press, Oxford, 1999).

[107] K. Kiuchi, Y. Sekiguchi, M. Shibata, and K. Taniguchi, Exploring Binary-Neutron-Star-Merger Scenario of Short-Gamma-Ray Bursts by Gravitational-Wave Observation, Phys. Rev. Lett. **104**, 141101 (2010).

[108] L. Rezzolla, L. Baiotti, B. Giacomazzo, D. Link, and J. A. Font, Accurate evolutions of unequal-mass neutron-star binaries: properties of the torus and short GRB engines, Classical Quantum Gravity **27**, 114105 (2010).

[109] I. H. Stairs, Pulsars in binary systems: Probing binary stellar evolution and general relativity, Science **304**, 547 (2004).

[110] K. Kyutoku, K. Ioka, H. Okawa, M. Shibata, and K. Taniguchi, Dynamical mass ejection from black hole-neutron star binaries, arXiv:1502.05402.

[111] J. E. McClintock, R. Narayan, and J. F. Steiner, Black hole spin via continuum fitting and the role of spin in powering transient jets, Space Sci. Rev. **183**, 295 (2014).

[112] Z. B. Etienne, Y. T. Liu, V. Paschalidis, and S. L. Shapiro, General relativistic simulations of black hole-neutron star mergers: Effects of magnetic fields, Phys. Rev. D **85**, 064029 (2012).

[113] F. Galeazzi, W. Kastaun, L. Rezzolla, and J. A. Font, Implementation of a simplified approach to radiative transfer in general relativity, Phys. Rev. D **88**, 064009 (2013).